Two-dimensional Vlasov simulation of electron plasma wave trapping, wavefront bowing, self-focusing, and sideloss[a)]

J. W. Banks,[1,b)] R. L. Berger,[1,c)] S. Brunner,[2,d)] B. I. Cohen,[1,e)] and J. A. F. Hittinger[1,f)]
[1]*Lawrence Livermore National Laboratory, Livermore, California 94551, USA*
[2]*Centre de Recherches en Physique des Plasmas, École Polytechnique Fédérale de Lausanne, Lausanne, Switzerland*

(Received 25 December 2010; accepted 14 March 2011; published online 9 May 2011)

Two-dimensional Vlasov simulations of nonlinear electron plasma waves are presented, in which the interplay of linear and nonlinear kinetic effects is evident. The plasma wave is created with an external traveling wave potential with a transverse envelope of width Δy such that thermal electrons transit the wave in a "sideloss" time, $t_{sl} \sim \Delta y/v_e$. Here, v_e is the electron thermal velocity. The quasisteady distribution of trapped electrons and its self-consistent plasma wave are studied after the external field is turned off. In cases of particular interest, the bounce frequency, $\omega_{be} = k\sqrt{e\phi/m_e}$, satisfies the trapping condition $\omega_{be}t_{sl} > 2\pi$ such that the wave frequency is nonlinearly downshifted by an amount proportional to the number of trapped electrons. Here, k is the wavenumber of the plasma wave and ϕ is its electric potential. For sufficiently short times, the magnitude of the negative frequency shift is a local function of ϕ. Because the trapping frequency shift is negative, the phase of the wave on axis lags the off-axis phase if the trapping nonlinearity dominates linear wave diffraction. In this case, the phasefronts are curved in a focusing sense. In the opposite limit, the phasefronts are curved in a defocusing sense. Analysis and simulations in which the wave amplitude and transverse width are varied establish criteria for the development of each type of wavefront. The damping and trapped-electron-induced focusing of the finite-amplitude electron plasma wave are also simulated. The damping rate of the field energy of the wave is found to be about the sideloss rate, $\nu_e \sim t_{sl}^{-1}$. For large wave amplitudes or widths Δy, a trapping-induced self-focusing of the wave is demonstrated. © *2011 American Institute of Physics*. [doi:10.1063/1.3577784]

I. INTRODUCTION

The dynamics of finite-amplitude electron plasma waves (EPWs) is rich in interesting phenomena and has received much attention in experiments,[1,2] theory,[3–6] and computer simulation.[7–9] In stimulated Raman backscattering (SRS), finite-amplitude electron plasma waves are responsible for scattering an incident electromagnetic wave into a backscattered electromagnetic wave.[10,11] EPWs, produced by the two-plasmon decay instability,[12] are important in both direct-drive inertial confinement fusion[13] and hohlraums,[14] where the high energy electrons accelerated by the EPW may have deleterious effects on the implosion. SRS is vitally important to indirect-drive inertial confinement fusion (ICF),[15,16] where recent experiments at the National Ignition Facility (NIF) have shown significant backscatter.[17,18]

SRS was studied systematically and modeled extensively in experiments with well-characterized plasma conditions and laser intensities of interest to NIF experiments.[19,20] The results of these experiments provided a database for theoretical modeling that is used for predicting backscattering of the laser light for NIF ignition campaign experiments.[21] Laser plasma instabilities, such as SRS and two-plasmon decay, place constraints on the ICF ignition designs that require compromises between the optimal parameters for implosions and for minimizing plasma instabilities.[22] In addition to ICF, SRS offers the intriguing possibility of producing ultrashort pulses of relativistically intense light by scattering long-pulse, low-intensity laser light from moderate amplitude EPWs.[23] The onset intensity and scaling of SRS have been modeled remarkably well with simulation codes[24] that neglect nonlinear and kinetic effects on the EPWs, despite the fact that these very simulations have EPW amplitudes that trap a significant number of electrons.[25] However, such codes are not as successful at predicting the levels of SRS in the strongly nonlinear limit when the damping, dispersion, and distortion of the EPW influence Raman scattering in important ways.

Nonlinear limitations on the effectiveness of large amplitude electron plasma waves in SRS backscattering laser light have been considered since the earliest experiments. The Langmuir decay instability,[26–28] for example, involves the backscatter of the large amplitude EPW by an ion acoustic wave. In NIF plasma conditions, that process is inhibited by the large damping rate of ion acoustic waves in helium and hydrocarbon plasmas. Recent work has shown that the longitudinal[29] and transverse trapped electron modulational

[a)]This work was performed under the auspices of the U.S. Department of Energy by Lawrence Livermore National Laboratory under contract number DE-AC52-07NA27344. This work was funded by the Laboratory Directed Research and Development Program at LLNL under project tracking code 08-ERD-031.
[b)]Electronic mail: banks20@llnl.gov.
[c)]Electronic mail: berger5@llnl.gov.
[d)]Electronic mail: stephan.brunner@epfl.ch.
[e)]Electronic mail: cohen1@llnl.gov.
[f)]Electronic mail: hittinger1@llnl.gov.

instablities[30] are effective in limiting the amplitude and coherence of the EPW. Because the EPW is produced in a laser speckle, it is born with a transverse modulation that can grow and filament under certain conditions.[31,32] The longitudinal modulations must grow from weaker perturbations. Rose has investigated the modulational stability of EPWs in the presence of trapped electrons with two-dimensional perturbations, amplitude-dependent diffraction of the EPW, and the competition of the modulational instability with Langmuir wave decay instability.[31] Rose and Yin have studied the filamentation instability of a finite-amplitude EPW.[32] Recent SRS simulations have shown how the filamentation of the EPW can limit the SRS.[30] The fundamental underlying physics responsible for the EPW phenomena in the aforementioned studies of Rose, Yin and co-workers, viz., finite-amplitude, kinetic effects on EPW dispersion and propagation in the presence of electron trapping, is examined from another perspective in the analysis and simulations presented here.

Motivated by the important kinetic effects of finite-amplitude EPWs in SRS, in other instabilities, and in wave heating of plasma, we employ the useful tool of numerical simulation to understand more thoroughly the complex phenomena involved. Moreover, we simplify by limiting ourselves to the purely electrostatic problem of driven EPWs. Vlasov simulation provides a means of simulating plasma physics that is free of statistical noise inherent to particle methods,[33] albeit at a higher computational cost in most cases.[34–37] Here we report Vlasov simulations of finite-amplitude EPWs in two spatial and two velocity dimensions. We excite waves by introducing an external electric field that is additive to the self-consistent internal electric field satisfying Gauss's law. The externally imposed longitudinal electric field has the form,

$$E_x^{\text{ext}} = A(y)P(t)E_0\cos(kx-\omega_0 t), \tag{1}$$

where $A(y)$ is the transverse wave envelope,[38]

$$A(y) = \exp\left[-\frac{1}{2}\left(\frac{y}{\Delta y}\right)^2\right], \tag{2}$$

that is maximum at $y=0$ and where $P(t)$ is a temporal shape function,

$$P(t) = \begin{cases} \frac{1}{2}\left[1+\tanh\left(4\left(\frac{2t}{t_r}-1\right)\right)\right] & \text{if } t<t_r, \\ \frac{1}{2}\left[1-\tanh\left(4\left(\frac{2(t-t_d)}{t_r}-1\right)\right)\right] & \text{if } t_r \le t < t_r+t_d, \\ 0 & \text{otherwise.} \end{cases}$$

Our simulations are periodic and one wavelength long along the propagation axis. In our simulations, we use $k\lambda_{\text{De}} = 1/3$ and $\omega_0/\omega_{\text{pe}} = 1.200$, similar to recent SRS simulations[30] and experimental values.[19,20] The driving frequency chosen here is equal to the linear resonant frequency determined by kinetic theory for the value of $k\lambda_{\text{De}}$ because SRS tends to occur most efficiently for frequencies near the linear resonance. The resonant response to the drive is somewhat insensitive to the precise value of driving frequency for driver frequencies whose difference from the linear resonant frequency is less in magnitude than the damping rate of the Langmuir wave. After the external driving field is turned off, the plasma responds only to the electric field, $\mathbf{E} = -\nabla\phi$ where $\phi(x,y,t)$ satisfies Poisson's equation. Our simulations illustrate some of the interesting physics of EPW propagation in two spatial dimensions that include both linear diffraction and nonlinearities associated with the trapping of electrons.

We consider physical situations with a well-defined ordering and separation of timescales. The EPW oscillation time, $\propto \omega_0^{-1}$, is much shorter than the electron trapping period at the bottom of the potential well, $\propto \omega_{\text{be}}^{-1}$, in the frame of reference comoving with the phase velocity of the EPW. At this point, it is convenient to introduce other time scales of interest: the time at which the driven wave reaches its maximum amplitude, t_{peak}; the transit time of a thermal electron across the lateral size of the simulation, $t_T = L_y/v_e$; the time for diffractive spreading rate of the wave, t_2 obtained in Appendix A; and the sideloss time $t_{\text{sl}} = \Delta y/v_e$. Here, L_y is the transverse size of simulation and $t_2 = 1/\sqrt{3}\omega_{\text{pe}}\left(\frac{\Delta y}{\lambda_{\text{De}}}\right)^2\frac{\omega_k}{\omega_{\text{pe}}}$. In all cases of interest, $t_2 \gg t_{\text{sl}}$ because the EPW width is many electron Debye lengths, i.e., $\Delta y \gg \lambda_{\text{De}}$. The transit time, t_T, is less than the diffraction time if $\Delta y > \sqrt{\lambda_{\text{De}}L_y}$. In our applications, the time scales obey the inequalities: $t_b < t_{\text{peak}}, t_{\text{sl}} < t_T, t_2$.

In our simulations, the EPW evolution is studied after the external field Eq. (1) is turned off, that is, for $t > t_r + t_d$. For a plane wave with periodic transverse boundary conditions, the EPW at this time would be an undamped, quasi-BGK wave with a frequency negatively shifted from the linear dispersion value.[4,5,39] The amplitude of the wave when the drive is turned off may be limited by the detuning of the resonance because of the nonlinear frequency shift. However, in simulations discussed in this paper, the external field has been turned off before detuning has an effect; thus $t_{\text{peak}} = t_r + t_d$.

When a strongly nonlinear EPW is excited by an external field with finite lateral extent, such as Eq. (2), the resulting EPW has its largest amplitude on axis (i.e., $y=0$). The trapping and concomitant nonlinear frequency shifts are weaker laterally off axis. Given that the nonlinear frequency shift due to trapping is negative, the lateral dependence of the frequency shift and the associated wave phase velocity lead to phasefronts, if certain conditions are met, that are curved in a focusing sense that we will refer to as nonlinear wavefront bowing.[40] Nonlinear wavefront bowing is illustrated in figures displayed in Sec. III.

In the linear analysis (Appendix) of the propagation of an EPW, a wave localized in the plane transverse to the propagation direction will diffract and have maximally curved wavefronts in a defocusing sense at a time, $t_{\max} = t_2/\sqrt{3}$. In Sec. III, a criterion is established for the establishment of nonlinear bowing by comparing the focusing curvature produced by nonlinear frequency shifts at $t_{\max}$ to the maximally curved defocusing linear wavefronts. Our Vlasov simulations establish the validity of this estimate. Our analysis and simulations quantify the linear and nonlinear wavefront bowing

physics regimes and provide insight into the wavefront bowing reported by Yin *et al.* in the simulation studies of stimulated Raman backscatter.[40,41]

Because of the spatial profile of the driver, the EPW frequency shift is a function of its transverse location for times less than the sideloss time, the simulation lateral transit time, and the time for diffractive spreading rate of the wave. Boundary conditions influence the results after either the lateral transit time or the time for wave diffraction to encounter the lateral boundaries, whichever is shorter.

The simulations also allow us to study other two-dimensional aspects of the EPW dynamics. Although the trapping of electrons can flatten the electron velocity distribution near resonance and can nonlinearly reduce electron Landau damping,[42] some of the Landau damping can be restored by undisturbed plasma that flows laterally into the domain of the EPW from the boundaries. The loss of trapped electrons from the wave leads to "residual" damping of the EPW, $\nu_{\mathrm{sl}} \propto t_{\mathrm{sl}}^{-1}$, such that, after the drive turns off, the wave loses energy to the transiting electrons. If outgoing BCs are applied such that incoming electrons are sampled from an unperturbed distribution, e.g., a Maxwell–Boltzmann distribution, the wave continues to decay with time, and the trapping regions also shrink with time. Eventually linear Landau damping is re-established. If periodic boundary conditions (BCs) are applied, this loss ceases when $t > t_T$. In addition, with periodic BCs, an EPW can evolve to have a perturbed electron velocity distribution that is nearly uniform laterally. In this circumstance, we observe that there is a nonlinear frequency shift that is likewise laterally uniform so that there is no further evolution of nonlinear bowing. Thus, the lateral boundary conditions can have a marked influence on the EPW propagation. The laterally outgoing BC on the distribution function is appropriate for EPWs driven by the ponderomotive force of a single laser speckle,[43] if the light wave is below the filamentation threshold. The periodic BC is more appropriate for the many-speckle case that is typical of most ICF experiments.[18,19]

Although the EPW field energy drops once the external field is turned off, the amplitude of the wave on axis does not if the trapping condition is met. Because of the focusing nature of the nonlinear phasefronts, one expects the EPW amplitude on axis to increase. For most of our simulations, this tendency is overcome by the loss of trapped electrons. However, we have clearly demonstrated in Sec. IV such trapped-electron-induced focusing when the sideloss rate was minimized.

The paper is organized as follows. In Sec. II, we describe the numerical algorithm used in our Vlasov–Poisson simulations. In Sec. III, we present the results of simulations and accompanying analysis that address the effects of finite amplitudes, electron trapping, and linear diffraction on the frequency of the plasma wave and on the curvature of the wave fronts. We examine the effects of trapping and lateral transit of electrons across a localized plasma wave on the self-focusing and damping of the wave in Sec. IV. Conclusions and discussion are presented in Sec. V. Simplified analytical models of linear and nonlinear wavebowing for an undriven EPW are given in Appendix A.

II. APPROACH

Consider the time evolution of a collisionless plasma in two space and two velocity dimensions with a stationary background of neutralizing ions. Furthermore, assume the nonrelativistic and electrostatic limits. Such a plasma is well described by the Vlasov–Poisson system,

$$\frac{\partial f}{\partial t} + v_x \frac{\partial f}{\partial x} + v_y \frac{\partial f}{\partial y} - E_x \frac{\partial f}{\partial v_x} - E_y \frac{\partial f}{\partial v_y} = 0, \tag{3}$$

$$E_x = -\frac{\partial \phi}{\partial x} + E_x^{\mathrm{ext}}, \quad E_y = -\frac{\partial \phi}{\partial y}, \tag{4}$$

$$\frac{\partial^2 \phi}{\partial x^2} + \frac{\partial^2 \phi}{\partial y^2} = \int_{-\infty}^{\infty}\int_{-\infty}^{\infty} f\, dv_x dv_y - 1 = \rho. \tag{5}$$

Here $f(x, y, v_x, v_y)$ is the electron distribution function; E_x and E_y are the x- and y-coordinates of the electric field, respectively; E_x^{ext} is the externally applied electric field; and ϕ is the electric potential. Distance has been normalized by the Debye length, velocity by the thermal velocity, time by the plasma frequency, and the electric field by $T_e/(e\lambda_{\mathrm{De}})$. The domain is artificially truncated in the velocity dimensions using $v_x \in [v_{x_{\min}}, v_{x_{\max}}]$ and $v_y \in [v_{y_{\min}}, v_{y_{\max}}]$, and a characteristic boundary condition are applied. The physical space domain uses $x \in [-L_x, L_x]$ and $y \in [-L_y, L_y]$. For the problems presented in this manuscript, periodic conditions are applied in the x-direction. For the y-direction, either periodic or characteristic boundary conditions are applied for the distribution function $f(x, y, v_x, v_y, t)$, while a periodic condition is always applied to the Poisson equation. For cases where a characteristic boundary condition is applied, incoming characteristics carry an undisturbed Maxwellian distribution.

Numerical approximation of Eqs. (3) through (5) follows an Eulerian finite-volume approach. Phase space is divided into cells using a Cartesian grid with mesh spacings Δx, Δy, Δv_x, and Δv_y. The Vlasov equation (3) is discretized using the conservative fourth-order finite-volume scheme introduced in earlier work.[44,45] Integrating (3) over a phase-space cell yields the system of ordinary differential equations (ODEs),

$$\begin{aligned}\frac{d}{dt}\bar{f}_{ijkl} &= -\frac{1}{\Delta x \Delta y \Delta v_x \Delta v_y}\int_{V_{ijkl}} \nabla \cdot \mathbf{F} dx\, dy\, dv_x dv_y, \\ &= -\frac{1}{\Delta x}\left(\langle F_x\rangle_{i+\frac{1}{2},jkl} - \langle F_x\rangle_{i-\frac{1}{2},jkl}\right) \\ &\quad -\frac{1}{\Delta y}\left(\langle F_y\rangle_{i,j+\frac{1}{2},kl} - \langle F_y\rangle_{i,j-\frac{1}{2},kl}\right) \\ &\quad -\frac{1}{\Delta v_x}\left(\langle F_{v_x}\rangle_{ij,k+\frac{1}{2},l} - \langle F_{v_x}\rangle_{ij,k-\frac{1}{2},l}\right) \\ &\quad -\frac{1}{\Delta v_y}\left(\langle F_{v_y}\rangle_{ijk,l+\frac{1}{2}} - \langle F_{v_y}\rangle_{ijk,l-\frac{1}{2}}\right).\end{aligned} \tag{6}$$

Here $\bar{f}_{ijkl}$ is the average distribution function over the cell-centered about $(x_i, y_j, v_{x_k}, v_{y_l})$, the angle braces indicate face average quantities, and $\mathbf{F} = (F_x, F_y, F_{v_x}, F_{v_y})$ are numerical fluxes at cell boundaries. High-order approximations of the numerical fluxes can be achieved by using high-order approximations of the cell-face averages.[44,45] For example,

$$\langle F_x\rangle_{i+\frac{1}{2},jkl} \approx \langle v_x\rangle_{i+\frac{1}{2},jkl}\langle f\rangle_{i+\frac{1}{2},jkl} + \frac{\Delta v_x}{24}\left(\langle f\rangle_{i+\frac{1}{2},j+1,kl} - \langle f\rangle_{i+\frac{1}{2},j-1,kl}\right). \tag{7}$$

In order to determine the needed face-averaged quantities of the distribution function, we use a nonlinear algorithm that adapts the stencil so as to control numerical oscillations.[46] For example, the average about the cell face $(i+\frac{1}{2},jkl)$ is defined using a weighted average of two third-order averages $\langle f\rangle^{(L)}_{i+\frac{1}{2},jkl}$ and $\langle f\rangle^{(R)}_{i+\frac{1}{2},jkl}$ as in

$$\langle f\rangle_{i+\frac{1}{2},jkl} = w^{(L)}_{i+\frac{1}{2},jkl}\langle f\rangle^{(L)}_{i+\frac{1}{2},jkl} + w^{(R)}_{i+\frac{1}{2},jkl}\langle f\rangle^{(R)}_{i+\frac{1}{2},jkl}. \tag{8}$$

The third-order averages are defined as

$$\langle f\rangle^{(L)}_{i+\frac{1}{2},jkl} = \frac{1}{6}\left(-\bar{f}_{i-1,jkl} + 5\bar{f}_{ijkl} + 2\bar{f}_{i+1,jkl}\right) \tag{9}$$

$$\langle f\rangle^{(R)}_{i+\frac{1}{2},jkl} = \frac{1}{6}\left(2\bar{f}_{ijkl} + 5\bar{f}_{i+1,jkl} - \bar{f}_{i+2,jkl}\right). \tag{10}$$

The weights are determined by

$$\text{if}\left(\langle v_x\rangle_{i+\frac{1}{2},jkl} > 0\right), \quad \begin{cases} w^{(L)}_{i+\frac{1}{2},jkl} = \max(w^{(1)}_{i+\frac{1}{2},jkl}, w^{(2)}_{i+\frac{1}{2},jkl}) \\ w^{(R)}_{i+\frac{1}{2},jkl} = \min(w^{(1)}_{i+\frac{1}{2},jkl}, w^{(2)}_{i+\frac{1}{2},jkl}) \end{cases} \tag{11}$$

$$\text{else} \quad \begin{cases} w^{(L)}_{i+\frac{1}{2},jkl} = \min(w^{(1)}_{i+\frac{1}{2},jkl}, w^{(2)}_{i+\frac{1}{2},jkl}) \\ w^{(R)}_{i+\frac{1}{2},jkl} = \max(w^{(1)}_{i+\frac{1}{2},jkl}, w^{(2)}_{i+\frac{1}{2},jkl}) \end{cases},$$

where $w^{(1)}_{i+\frac{1}{2},jkl}$ and $w^{(2)}_{i+\frac{1}{2},jkl}$ are the traditional WENO weights determined as in earlier work.[47,48] To evolve the set of ODEs in (6), we use the standard explicit fourth-order Runge–Kutta time discretization.[49]

Because cell-averaged quantities are directly time-advanced, the cell-averaged charge density used in the Poisson equation (5) is easily computed through summation,

$$\bar{\rho}_{ij} = \Delta v_x \Delta v_y \sum_{k=1}^{N_{vx}}\sum_{l=1}^{N_{vy}} \bar{f}_{ijkl} - 1. \tag{12}$$

Numerical approximation of the Poisson equation is then carried out on the cell-averaged densities directly using centered finite differences using the solvers in the Overture software package.[50,51] The discretization uses the centered fourth-order difference approximations giving,

$$\frac{-\bar{\phi}_{i+2,j} + 16\bar{\phi}_{i+1,j} - 30\bar{\phi}_{ij} + 16\bar{\phi}_{i-1,j} - \bar{\phi}_{i-2,j}}{\Delta x^2} + \frac{-\bar{\phi}_{i,j+2} + 16\bar{\phi}_{i,j+1} - 30\bar{\phi}_{ij} + 16\bar{\phi}_{i,j-1} - \bar{\phi}_{i,j-2}}{\Delta y^2} = \bar{\rho}_{ij}. \tag{13}$$

A direct LU (lower and upper triangular matrices)-decomposition of the resulting matrix is performed as a preprocessing step; thus, the solution of the Poisson system at each time step requires only a back substitution. Finally, cell-average values of the electric field are derived from cell-averages of the electric potential via fourth-order centered differences:

$$\bar{E}_{xij} \approx \frac{1}{12\Delta x}\left[8(\bar{\phi}_{i+1,j} - \bar{\phi}_{i-1,j}) - \bar{\phi}_{i+2,j} - \bar{\phi}_{i-2,j}\right]. \tag{14}$$

More details concerning the discretization are to be found in Banks and Hittinger.[46]

It is worth noting that, for the computations performed in this work, parallel processing on hundreds or thousands of processors was required. Our parallel decomposition performs a tensor product decomposition on the distribution function among all but a single processor. This last processor is reserved for the Poisson solve. This decomposition strategy has worked well and provides excellent parallel scaling for the simulations presented here, but will require some modification as the problem sizes grow further. At some size, the Poisson solve must also be distributed in parallel, and the direct LU-decomposition we perform here will no longer be viable. Instead, an iterative linear solver such as GMRES (generalized minimal residual method) will be employed.[52] Our preliminary studies indicate that this approach works well; only two or three coupling iterations are required to achieve convergence. More detailed studies of issues relating to parallelization will be the subject of future work.

III. EFFECTS OF TRAPPING AND DIFFRACTION ON PLASMA WAVE PROPAGATION

In this section, we report simulation results that illustrate electron plasma wave nonlinearities associated with electron trapping phenomena in one and two spatial dimensions. We first report observations of nonlinear frequency shifts in two spatial dimensions. We follow this with a discussion of how linear and nonlinear effects influence wavefront curvature in two spatial dimensions.

A. Nonlinear frequency shift due to electron trapping in two spatial dimensions

We first note that, in physical circumstances, EPWs are inevitably localized in space. In ICF experiments at the National Ignition Facility, large amplitude EPWs are created by stimulated Raman backscattering in laser beams with intensity $\lesssim 10^{15}$ W/cm^2 with a focal spot diameter of $\sim$0.5 mm. However, the NIF focal spot consists of thousands of intense speckles of transverse size of order $f_s\lambda_0 \sim 3\times 10^{-4}$ cm, where f_s is the f-number of the lens and λ_0 is the vacuum wavelength of the laser light, viz., 351 nm. Since SRS is a nonlinear process, the backscattered light and the associated EPWs are also localized in the laser speckles. The simulation results presented here illustrate some aspects of two-dimensional localization and trapping on EPW propagation.

For finite wave amplitude, there are nonlinear frequency shifts from trapping that are proportional to $\sqrt{\phi}$ and quadratic nonlinearities, ϕ^2.[53] Both nonlinearities are naturally present in Vlasov simulations. For an EPW, the quadratic nonlinearity leads to a positive frequency shift.[54,55] For small wave amplitudes, the case of interest in this paper, the

square-root nonlinearity dominates the quadratic fluid nonlinearity if $k\lambda_{De} \gtrsim 0.25$ and $e\phi/T_e < 1$. Recently, comparison of fluid and kinetic effects on EPW frequency shifts has shown that, even though smaller, fluid shifts can play an important role.[56]

The magnitude of the frequency shift and the distribution of the trapped electrons depend on the details of the process that creates the EPW. Two limiting cases have been treated analytically. Dewar's calculation[4] of the nonlinear frequency shift accounts for whether the wave is turned on "suddenly" or "adiabatically," which affects the distribution in energy of the resonant electrons, trapped and untrapped. In both cases, the frequency shift is found to be

$$\frac{\Delta\omega_{nl}}{\omega_{pe}} = -\frac{\alpha}{(k\lambda_{De})^3}\left(\frac{\delta n}{n}\right)^{1/2}\left(\frac{1}{2\pi}\right)^{1/2}(v^2-1)\exp\left(-\frac{v^2}{2}\right), \tag{15}$$

where $v = \omega/kv_{th}$, $|\delta n/n| = k^2\lambda_{De}^2|e\phi/T_e|$ is the relative electron density perturbation in the EPW, and $\alpha = 0.544$ (adiabatic wave turn on) or 0.823 (sudden wave turn on). Vlasov simulations of the nonlinear frequency shift of an EPW due to electron trapping and of an ion acoustic wave due to electron and ion trapping have shown in 1D that the frequency shift follows the "sudden" or "adiabatic" relation if the wave is initialized at finite amplitude or driven slowly to its final amplitude, respectively.[57] Defining the condition for "sudden" as $\int_0^{t_{peak}} \omega_b(t)dt < 2\pi$ and assuming that the wave grows at most linearly with t, we obtain the condition, $\omega_b(t_{peak})t_{peak} < 3\pi$ where the bounce frequency $\omega_b = k\lambda_{De}\sqrt{e\phi/T_e}\,\omega_{pe}$. In terms of the wave amplitude, this condition for the sudden approximation, $e\phi(t_{peak})/T_e < (3\pi/(k\lambda_{De}\omega_{pe}t_{peak}))^2$, is well satisfied even for the largest fields in our simulations.

The condition describing whether the wave is excited suddenly or adiabatically acquires a dependence on transverse position y through the dependence of the EPW amplitude on lateral position y. If the EPW amplitude at a given location y is relatively constant over a time exceeding two trapping periods, then the theories of Morales and O'Neil[5] and Dewar[4] are applicable in describing the nonlinear frequency shift in the EPW due to trapping. There has been much additional work on the calculation of the nonlinear dispersion relation for an EPW when driven and in particular, when driven by stimulated Raman scattering, e.g., the studies of Rose and Russell[39] and more recently by Benisti *et al.*[58–60] Rose and Russell[39] obtain a nonlinear frequency shift that is close to the value determined in the sudden approximation by Morales and O'Neil[5] and by Dewar.[4] Benisti *et al.* consider freely-propagating and driven waves in the adiabatic limit and emphasize circumstances in which the driving of the EPW is determined directly by stimulated Raman scattering.[58–60] For a freely-propagating EPW in the adiabatic limit and for $k\lambda_{De} = 0.35$, Benisti *et al.*[58] obtain frequency shifts as a function of amplitude that are slightly larger in magnitude than the adiabatic result of Dewar[4] and generally track Dewar's formula. For larger values of $k\lambda_{De}$, Benisti *et al.*'s results are relatively larger in magnitude than Dewar's adiabatic result.[59]

In the simulations, the frequency of the EPW was obtained at several different lateral positions to verify the predicted dependence of the phase velocity on the wave amplitude. The external field wavenumber and frequency were, respectively, $k\lambda_{De} = 1/3$ and $\omega_0/\omega_{pe} = 1.200$ for the sake of specificity, which is the linear kinetic normal mode frequency. The nonlinear frequency shifts were calculated well after the external field was zero, i.e., for $t > t_r + t_d = 50/\omega_{pe}$. A Hilbert transform of the field time dependence at a specified spatial location over a time interval, typically $100 < \omega_{pe}t < 300$, is done to obtain the frequency in the nonlinear state.[61] Frequency shifts, the frequency from the transform minus the driver frequency, are plotted as a function of wave amplitude in Fig. 1. With one exception, the transverse boundaries in y were set far enough away from the central axis to have little effect for $\omega_{pe}t \leq 300$.

The simulation data in Fig. 1 tracks the $\sqrt{\phi}$ scaling very well, and all the simulations are in the sudden turn-on regime. In 2D with periodic boundary conditions and times less than the transit time of a thermal electron across the wave, the velocity distribution functions retain their dependence on y. The frequency shifts obtained from off axis, where the wave amplitude is weaker, are smaller in value as expected. In all of our simulations except for the largest amplitude wave shown in Fig. 1, the fluid frequency shift[56] is insignificant.

In simulations with periodic boundary conditions in y and at times larger than t_T, the transit time of a thermal electron across the system, the resonant electron distribution becomes uniform laterally. This results in the nonlinear frequency shift losing its spatial dependence on the local value of ϕ and y, although the wave amplitude retains a dependence on y. The frequency shifts with red crosses in Fig. 1 are

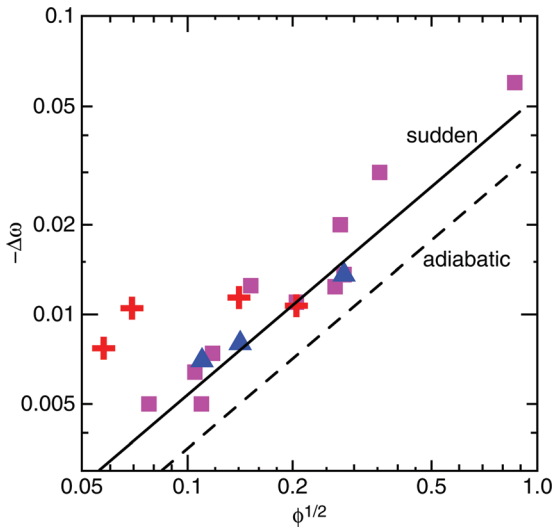

FIG. 1. (Color online) Nonlinear frequency shifts vs square-root of wave amplitude $|e\phi/T_e|^{1/2}$, for laterally periodic boundary conditions. The squares are frequency shifts determined on axis. The blue triangles and red crosses are for different lateral positions. The blue data is for the wide driver case where the nonlinear shifts are dominant and the measurements were made for a time interval before a thermal transit time across the wave. The red crosses for a narrow driver run long enough so that the resonant electrons have the same distribution for all y. Thus, the frequency shift (red crosses) is nearly independent of the local field, ϕ.

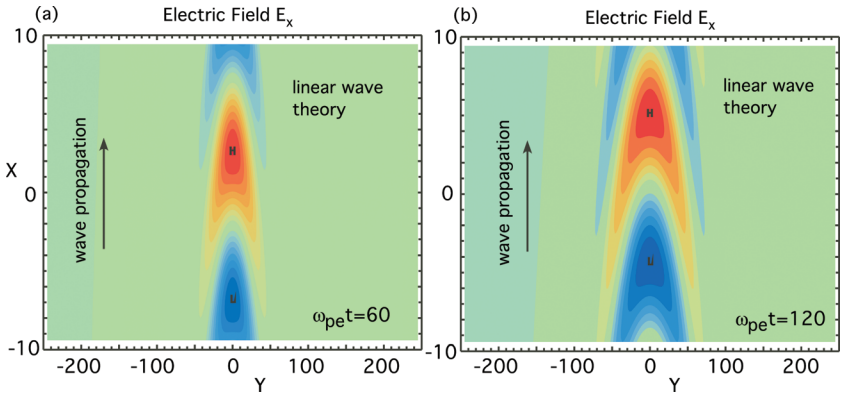

FIG. 2. (Color online) Plot of electric field contours at fixed times (a) $\omega_{pe}t = 60$ and (b) $\omega_{pe}t = 120$ with $\Delta y/\lambda_{De} = 12$ showing evolution of wavefront bowing from linear theory.

taken at the different lateral positions $y/\lambda_{De} = 3.9$, 59, 98, 122 over the time interval $\omega_{pe}t = [100, 300]$ when the trapped electron distribution has become more uniform. In this case, $t_T = 251\omega_{pe}^{-1}$ and $\Delta y = 31.4\lambda_{De}$. The frequency shifts are then dependent on the wave amplitude at earlier times and at other positions, i.e., there is a nonlocal dependence of frequency shift on wave amplitude. One should compare this narrow driver case to the wider driver case where the frequency shift for different lateral positions (blue triangles) is consistent with the local value of ϕ. In most cases, the wider driver case is the one of physical interest.

B. Wavefront bowing

Nonlinear wavefront bowing is a significant feature in 2D and 3D PIC simulations of stimulated Raman backscatter in transversely localized electromagnetic fields.[40,41] A simplified analysis of wavefront bowing for a large-amplitude EPW with a transverse amplitude dependence that is peaked on axis is provided in Appendix A. This analysis compares the 2D constant phase surfaces with curvature determined by linear diffraction to surfaces with curvature determined by the nonlinear frequency shift. The curvature for linear wavefront bowing is found to be

$$C_l = -\frac{\frac{3}{2}\left(\frac{\lambda_{De}}{\Delta y}\right)^2\frac{\omega_{pe}}{\omega_k}\omega_{pe}t}{1+9\left(\frac{\lambda_{De}}{\Delta y}\right)^4\frac{\omega_{pe}^2}{\omega_k^2}\omega_{pe}^2t^2} \tag{16}$$

while that due to the nonlinear bowing is

$$C_{nl} = -\frac{1}{4}\frac{\Delta\omega_{nl}}{\omega_{pe}}\omega_{pe}t, \tag{17}$$

where Δy is a measure of the initial transverse width of the EPW envelope [see Eq. (2)], $\omega_k = \omega_{pe}(1+3k^2\lambda_{De}^2)^{1/2}$ is the linear Bohm–Gross frequency, and $\Delta\omega_{nl}$ is given in Eq. (15). Because $\Delta\omega_{nl} < 0$, the curvatures have opposite signs ($C_l < 0$, $C_{nl} > 0$), and both grow initially in time as $\omega_{pe}t$. The wave forms suggested by this analysis are plotted in Fig. 2 for small-amplitude waves and in Fig. 3 for large-amplitude waves in the trapping-dominated regime. Of course, this analysis is limited in that it neglects damping, assumes an infinite homogeneous domain, and uses the wave amplitude as a parameter in the nonlinear calculation.

The linear curvature peaks at a value max $(C_l) = -1/4$ at a time t_{max} determined by

$$3\left(\frac{\lambda_{De}}{\Delta y}\right)^2\frac{\omega_{pe}}{\omega_k}\omega_{pe}t_{max} = 1. \tag{18}$$

If $C_{nl} \gg |C_l|$ for $t \ll t_{max}$, then $C_{nl} \gg |C_l|$ for all time, which is equivalent to

$$\frac{1}{4}\left|\frac{\Delta\omega_{nl}}{\omega_{pe}}\right| \gg \frac{3}{2}\left(\frac{\lambda_{De}}{\Delta y}\right)^2\frac{\omega_{pe}}{\omega_k}. \tag{19}$$

When Eq. (19) is satisfied, the trapping nonlinearity is dominant, and the wavefront is nonlinear. In the opposite limit of Eq. (19), linear bowing is initially dominant but relaxes in time. Thus the wave front curvature can change sign depending on the evolution of the wave amplitude. For times much

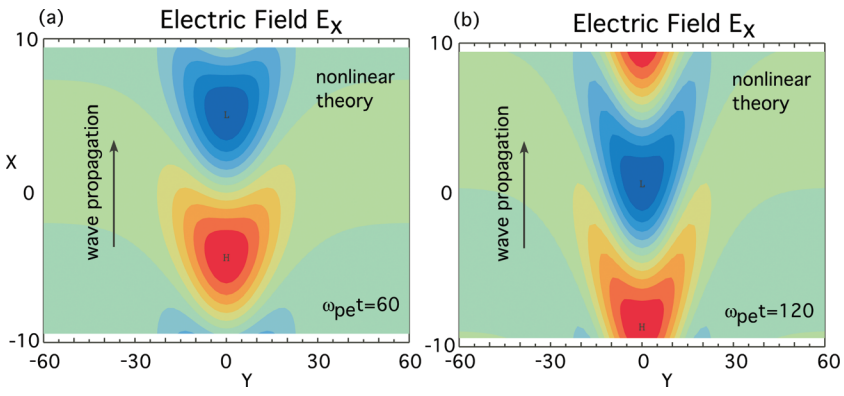

FIG. 3. (Color online) Plot of electric field contours at fixed times (a) $\omega_{pe}t = 60$ and (b) $\omega_{pe}t = 120$ with $\Delta y/\lambda_{De} = 12$ and $e\phi/T_e = 0.012$ initially on axis showing nonlinear wavefront bowing.

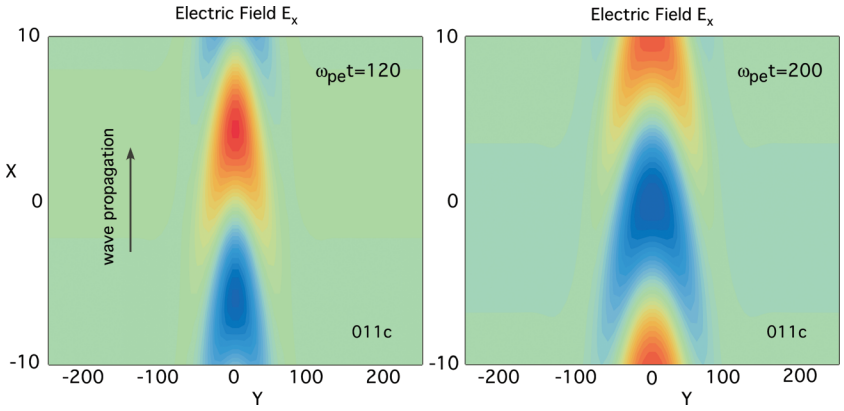

FIG. 4. (Color online) Plot of electric field contours at $\omega_{pe}t = 120$ and 200 showing wavefront bowing from a simulation with $\Delta y/\lambda_{De} = 12$ and peak wave amplitude $e\phi/T_e = 0.0024$ on axis which then steadily decreases.

greater than the time it takes a thermal electron to transit laterally across the simulation domain, the phase velocity is independent of y, the nonlinear bowing no longer evolves, and the wavefront pattern freezes.

Figures 4–6 display plots of the electric field from simulations of waves in the large and very small-amplitude physics regime, with peak wave amplitudes on axis $e\phi/T_e = 0.0024$, 0.081, and 0.075, respectively. (Other than the peak values of the driving amplitude and the width of the driving wave, the parameters used here are the same as those in the simulations contributing to Fig. 1.) The simulation in Fig. 6 uses a wide waveform, and the amplitude on axis remains near its peak amplitude over the duration of the simulation. The simulations in Figs. 4 and 5 have relatively narrow waveforms with wave amplitudes that relax to significantly smaller amplitudes on axis as the wave spreads. The simulation results can be compared qualitatively to the analytic results shown in Figs. 2 and 3. We note that the time duration of the wave driver in these simulations is $\sim 50\omega_{pe}^{-1}$, while the plots in Figs. 2 and 3 are for times in the theoretical model used with instantaneous wave turn on; thus, comparisons should be made between the theoretical models and the simulations with a time lag of $\sim 50\omega_{pe}^{-1}$ in the simulations. Quantitative comparison is inappropriate because the initial wave drive, the transverse boundaries, the effects associated with electron transit across the wave, and the finite wave damping in the simulations are not included in the analysis.

A measure of the relative nonlinearity expected in the wavefront bowing is to evaluate C_{nl} at the time when the linear curvature maximizes, i.e., Eq. (18), and compare it to the value of the maximum linear curvature,

$$C_{nl}(\omega_{pe}t_{max}) = \frac{1}{12}\left|\frac{\Delta\omega_{nl}}{\omega_{pe}}\right|\frac{\omega_k}{\omega_{pe}}\left(\frac{\Delta y}{\lambda_{De}}\right)^2 : |\max(C_l)| = 1/4. \tag{20}$$

Note the condition $C_{nl}(\omega_{pe}t_{max}) \gg 1/4$ from Eq. (20) differs from the condition in Eq. (19) precisely by a factor of two. For the simulation results in Figs. 4 and 5, $C_{nl}(\omega_{pe}t_{max}) = 0.02$ and 0.15, respectively, evaluated on axis at $\omega_{pe}t_{max} \sim 60$ after the termination of the drive when the wave amplitudes have decreased on axis substantially, i.e., $e\phi/T_e = 0.0003$ and 0.021. We observe that the physics in Fig. 4 is clearly linear, and the curvature tends to saturate for times exceeding $O(\omega_{pe}t_{max} = (\Delta y/\lambda_{De})^2(\omega_k/\omega_{pe})/3 \sim 60)$ after the driver is terminated. The curvature in Fig. 6 is in the highly nonlinear regime, $C_{nl} \gg |C_l|$. Because the wave is relatively wide and maintains its amplitude over the duration of the simulation, the nonlinear bowing and curvature continue to grow in time. Figures 4 and 6 compare qualitatively well to Figs. 2 and 3, respectively. In Fig. 5, there is some weak dimpling of the wave fronts near the axis at $\omega_{pe}t = 120$ that suggests that the trapping nonlinearity has a small, but finite influence. This dimpling grows into a more pronounced distortion visible at $\omega_{pe}t = 200$.

We conclude that the simulation shown in Fig. 4 is in a physics regime where linear dispersion is largely dominant in determining the wave front curvature, and the simulation compares qualitatively to the theoretical wavefronts in Fig. 2. The simulation shown in Fig. 6 with its larger width maintains its amplitude near the axis and remains in a physics regime where nonlinearity is determining the curvature. There is qualitative agreement between the wave fronts

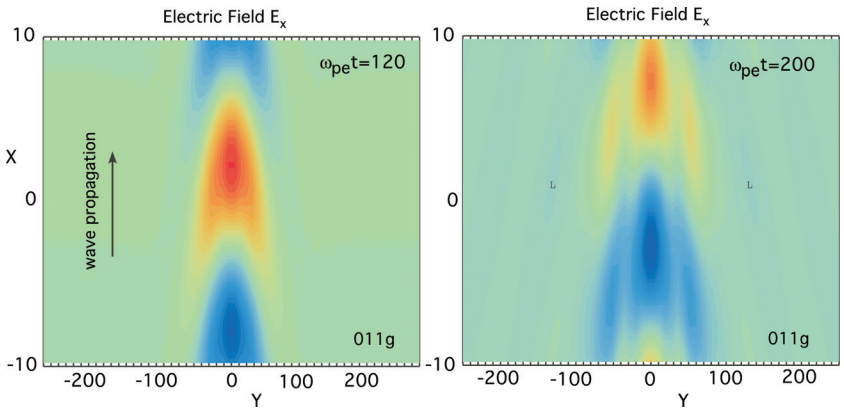

FIG. 5. (Color online) Plot of electric field contours at $\omega_{pe}t = 120$ and 200 showing wavefront bowing from simulation with $\Delta y/\lambda_{De} = 12$ peak wave amplitude $e\phi/T_e = 0.081$ on axis which then decreases.

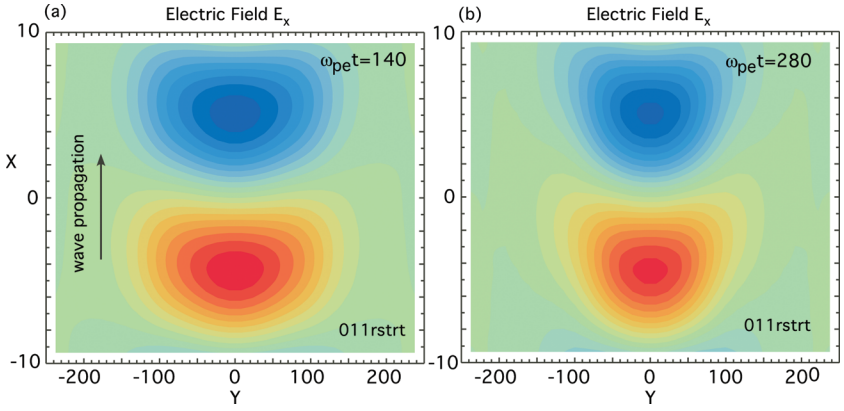

FIG. 6. (Color online) Plot of electric field contours at $\omega_{pe}t = 140$ and 280 showing wavefront bowing from simulation with $\Delta y/\lambda_{De} = 90$ and peak wave amplitude $e\phi/T_e = 0.075$ on axis whose amplitude is relatively stationary near the axis.

in Fig. 6 and the theoretical wave fronts shown in Fig. 3. Whether the wave curvature is positive or negative in our simulations (indicating physics dominated by nonlinear trapping or linear dispersion) is consistent with the conditions given in Eqs. (19) and (20). In addition, the estimate for the saturation time of the linear bowing, Eq. (18), is also useful in providing understanding of the simulations results.

In the stimulated Raman backscattering simulations shown in Fig. 1 of Yin *et al.*,[40] the parameters for the electron plasma wave correspond to $k\lambda_{De} = 0.34$, $\Delta y \sim 2\mu$m, and $\Delta y/\lambda_{De} = 1.3 \times 10^2$. Hence, $\omega_{pe}t_{max} = O(6 \times 10^3)$; and the comparison in Eq. (19) yields $O(10^{-2}) : O(10^{-4})$ for the relative magnitude of the nonlinear curvature compared to the linear curvature for $t \ll t_{max}$. One concludes that the wave curvature of the EPW in Fig. 1 of Yin *et al.*[40] is in the highly nonlinear regime exhibiting self-focusing curvature.

IV. FOCUSING AND DAMPING OF FIELDS FROM TRAPPED ELECTRONS

Consider an EPW wave with a finite transverse extent and consider electrons that transit through the wave transversely, become trapped, exchange energy with the wave and leave. Nonresonant electrons adiabatically acquire an oscillatory energy as they enter into the wave and give the energy back as they leave. In contrast, the resonant electrons, with a parallel velocity within a trapping velocity of the phase velocity, together remove a net amount of energy from the wave. That is, some electrons gain and some lose energy to the field but there is a net loss by the field. In this section, the rate of energy loss through convection is examined in some detail. Detrapping by electron–electron collisional drag and electron–ion pitch-angle scatter is not included in the Vlasov simulations nor in our theoretical estimates. Recent theory[62–64] has shown that, in cases of high importance, collisional detrapping is less important than convective loss for localized EPWs.

For wide enough wave shapes or strong enough wave amplitudes, the wavefronts develop a focusing curvature as a result of nonlinear bowing. If damping is neglected, this focusing would narrow the transverse shape of the field while increasing the field amplitude on axis consistent with wave energy conservation. However, the transiting, resonant electrons actually take energy from the wave field, which reduces the wave amplitude. Damping and focusing effects are thus in competition with respect to the evolution of the amplitude on axis. In all simulation results presented so far, the damping effect dominated the focusing on axis. In this section, we will, however, show an example wherein the transiting electron damping rate is slow enough that the field amplitude on axis increases even as the total field energy decreases with time. Theoretical analysis has identified the key parameter for energy loss through convection to be the number of bounce cycles in the interaction of resonant electrons with the wave. This number is given by the product of the bounce frequency and the sideloss time, $N_b = \omega_{be}t_{sl}/2\pi = k\lambda_{De}(\Delta y/2\pi\lambda_{De})\sqrt{e\phi/T_e} = k\lambda_{De}(w_{fw}/4\pi\sqrt{\ln 2}\lambda_{De})\sqrt{e\phi/T_e}$, where $w_{fw} \simeq 2\sqrt{\ln 2}\Delta y$ is the FWHM of the external field intensity. The case shown in Fig. 6, for example, has $w_{fw} = 160\lambda_{De}$ and $N_b = 1.3$ for the peak wave amplitude on axis. Other simulations, especially those with linear phase fronts, have bounce numbers less than one. For comparison of these parameters with a practical application, consider an EPW driven within a laser speckle of a NIF beam with lateral width, $f_s\lambda_0 = 2.8 \times 10^{-4}$ cm, where the f-number $f_s \approx 8$ and the laser wavelength $\lambda_0 = 351$ nm. For typical plasma parameters $T_e = 2.5$ keV and electron density $N_e = 0.1\ N_c$, where N_c is the critical density, $f_s\lambda_0/\lambda_{De} \sim 220$. Note, in our example, $k\lambda_{De} = 1/3$ is determined from the SRS matching conditions for these values of N_e and T_e.

As the bounce number increases, the physical system approaches the 1D limit where the Landau damping of a large-amplitude EPW decreases with time and where, after several bounce periods, a loss-free nonlinear wave is established.[65] That is, a quasi-BGK state is achieved in the limit that $w_{fw}/\lambda_{De} \to \infty$. In Fig. 7, a comparison of the evolution of the EPW for a wide spatial envelope, $w_{fw}/\lambda_{De} = 151$, is displayed for two different transverse boundary conditions on the electron distribution: periodic and outgoing. For the outgoing condition, outflow is handled through extrapolation and inflow is specified by an undisturbed Maxwellian with the same parameters as the initial distribution. In both cases, the total field energy, $W_E = \int_{x,y} |E^2(x,y)|dxdy$, decreases in time after the driving field turns off at $\omega_{pe}t = 50$. The two cases differ noticeably after $\omega_{pe}t = 220$, the time it takes a thermal electron to travel from the peak field to the boundary. In the periodic case, the loss of field energy to kinetic energy ceases at late times when the distribution of resonant electrons becomes more uniform laterally. For the outgoing boundary condition, the loss is monotonic. A different

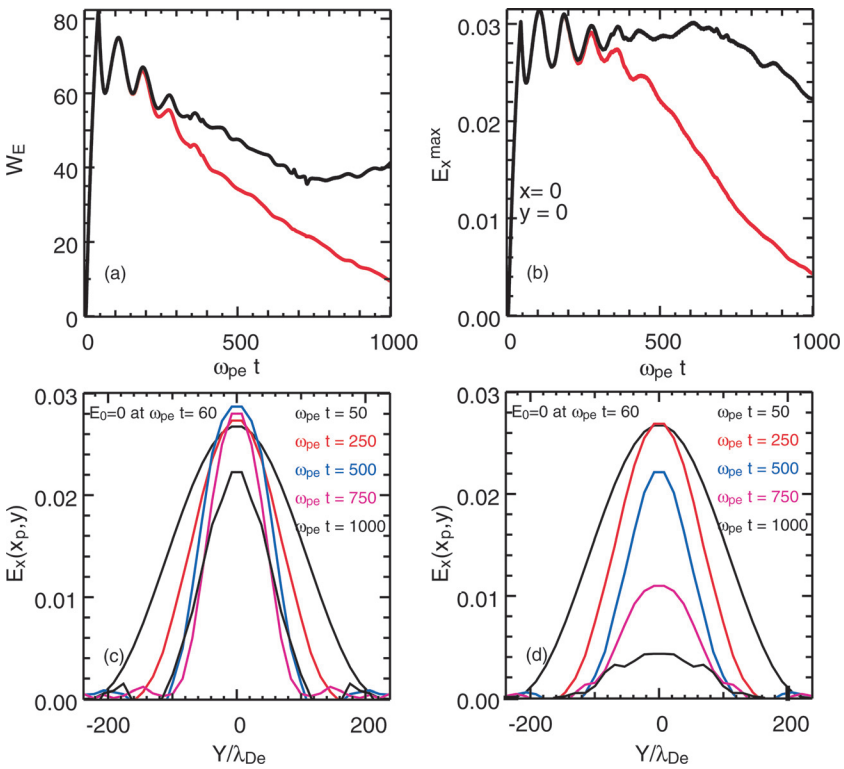

FIG. 7. (Color online) Comparison of the EPW field history for periodic and outgoing boundary conditions for the wide lateral shape, $w_{fw}/\lambda_{De} = 151$. The driving external field is turned off at $\omega_{pe}t = 50$. (a) The history of the EPW field energy, W_E, with periodic (black) and outgoing electron (red) boundary conditions. (b) The history of the peak EPW field with periodic (black) and outgoing electron (red) boundary conditions. (c) Transverse spatial dependence of $E_x(x_p, y)$ at five times for the periodic electron distribution boundary conditions. (d) Transverse spatial dependence of $E_x(x_p, y)$ at five times for the outgoing electron distribution boundary conditions. For (c) and (d), x_p is the position at which $E_x(x, y = 0)$ is maximum. Electric fields are normalized such that $E_{code} = e\lambda_{De}E/T_e$.

picture emerges when the history of maximum field amplitude (which is on the axis) is displayed. The maximum field amplitude actually increases slightly after the driver is off and, in the periodic case, maintains that amplitude until late in time. With outgoing boundary conditions the maximum decreases monotonically with time. When $t > t_T = 440$, the periodic boundary conditions affect the further evolution of the field. Also shown in Fig. 7, are lineouts of the transverse spatial dependence of the EPW field at the axial position where the field is maximum. In the periodic case, as the field amplitude increases slightly on axis, its width narrows. This result suggests an EPW self-focusing process. In the outgoing electron case, the EPW field narrows as well but the wave damping from the transverse loss rate overcomes the tendency of the field to grow on axis. The focusing effect of curved wavefronts is limited by two effects of the transiting electrons: (1) the loss of field energy to the resonant electrons that transit the wave and (2) the increasingly uniform trapping region. The first effect makes the condition in Eq. (19) more difficult to satisfy. The second reduces the transverse dependence of the frequency shift on the local wave amplitude.

For an EPW of $\sim 1/3$ the width of the previous example, $w_{fw} = 52\lambda_{De}$, and driven to the same amplitude at $\omega_{pe}t = 50$, the bounce number is $N_b \sim 0.5$. This case is shown in Fig. 8 where the maximum field amplitude drops quickly as soon as the driving field is turned off. The total width of the simulation is also smaller in this case, and $t_T = 125\omega_{pe}^{-1}$. The behavior of the periodic simulations differs from the outgoing electron simulations as soon as $t > t_d + t_T/2$, as was true of the field with the wider simulation size. The transverse spatial dependence of the field widens with time as the field decreases in amplitude. This spreading behavior is independent of the distribution boundary condition, although, of course, the rate of decrease of the field amplitude is slower with periodic boundary conditions

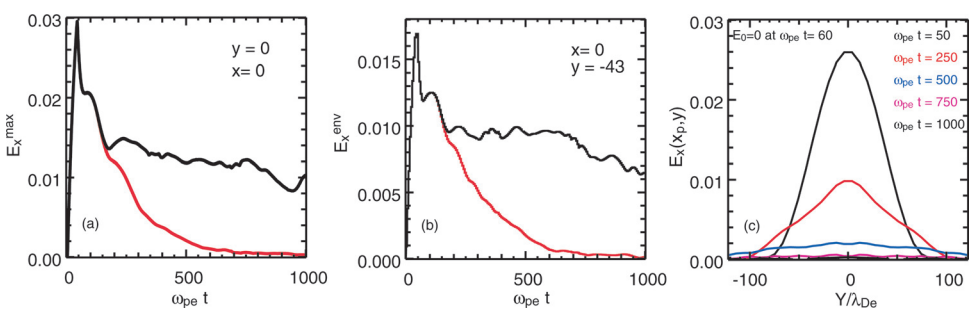

FIG. 8. (Color online) Comparison of the EPW field history for periodic and outgoing boundary conditions for a narrow lateral shape, $w_{fw}/\lambda_{De} = 52$. The driving external field is turned off at $\omega_{pe}t = 50$. (a) The history of the peak EPW field with periodic (black) and outgoing electron (red) boundary conditions. (b) The history of the EPW field envelope at $y = -43\lambda_{De}$ with periodic (black) and outgoing electron (red) boundary conditions. (c) Transverse spatial dependence of $E_x(x_p, y)$ at five times indicated for the outgoing electron distribution boundary conditions. Here, x_p is the position for which $E_x(x, y = 0)$ is a maximum.

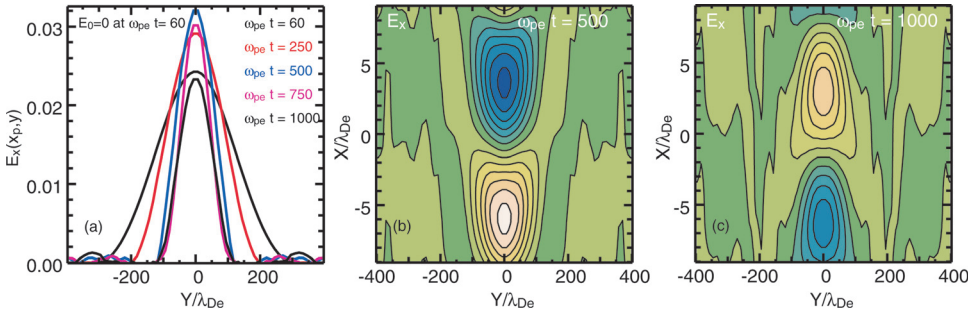

FIG. 9. (Color online) The EPW field for a lateral shape $w_{fw} = 201\lambda_{De}$. The driving external field is turned off at $\omega_{pe}t = 60$. (a) The transverse shape of the EPW at the axial position, x_p, where the field is a maximum for five times after the driving field is off. (b) Two-dimensional filled contour maps of the EPW field at the time of maximum focusing. (c) Two-dimensional filled contour maps of the EPW field after diffraction has overtaken focusing. There are 13 equally spaced contours in the range $[-0.03, 0.03]$ for both figures (b) and (c).

transverse to the propagation direction. The field transverse size and amplitude are small enough to have linear phase fronts at all times.

Focusing can be convincingly demonstrated by increasing the wave amplitude for a given width or by increasing the width to lower the loss rate of resonant electrons. For the second choice, consider a simulation with a transverse size of $804\lambda_{De}$, $t_T = 804\omega_{pe}^{-1}$, and width $w_{fw} = 201\lambda_{De}$ with periodic boundary conditions. In Fig. 9, transverse lineouts of the 2D field at the axial position where E_x is maximum are shown. At $\omega_{pe}t = 50$, when the drive turns off, the field shape is determined by the driving potential. After that time, the curved wave fronts cause the field to focus. A balance of focusing and diffraction occurs when $\omega_{pe}t = 500$ after which the maximum amplitude decreases. The 2D field at $\omega_{pe}t = 500$ in Fig. 9 shows nonlinear wavefront curvature. Later in time, the diffraction is dominant, and the wavefronts have linear curvature as also shown in Fig. 9. This behavior contradicts the analysis in Secs. A and III, which show that once nonlinear bowing is dominant it remains so. That analysis neglected damping by transiting electrons and the development of a transversely uniform trapping region also due to the transiting resonant electrons. The first effect reduces the magnitude of the frequency shift and makes the condition for nonlinear bowing in Eq. (19) harder to satisfy later in time. The second effect reduces the transverse dependence of the frequency shift on the local field amplitude.

It is instructive to view the evolution of the distribution function at these different epochs. In Fig. 10, the distribution of electrons in the trapped region at the maximum of the EPW potential ϕ is shown as a function of the axial velocity and the transverse position, and also as a function of the axial velocity and the axial position at the centerline in y. The distribution is integrated over the transverse velocity. The velocity distribution is also shown as a function of the axial velocity as lineouts at the peak of the EPW amplitude in x and at various values of y and times in Fig. 11. The transverse shape of the resonant electrons reflects the shape of the driving potential at $\omega_{pe}t = 50$ when the drive turns off. By $\omega_{pe}t = 250$, some accelerated electrons have reached the lateral edge of the simulation region and the shape of the trapped region has narrowed (not shown in the figure). At $\omega_{pe}t = 500$, a tail of electrons has appeared at the lateral boundaries and the trapped electrons occupy a narrower

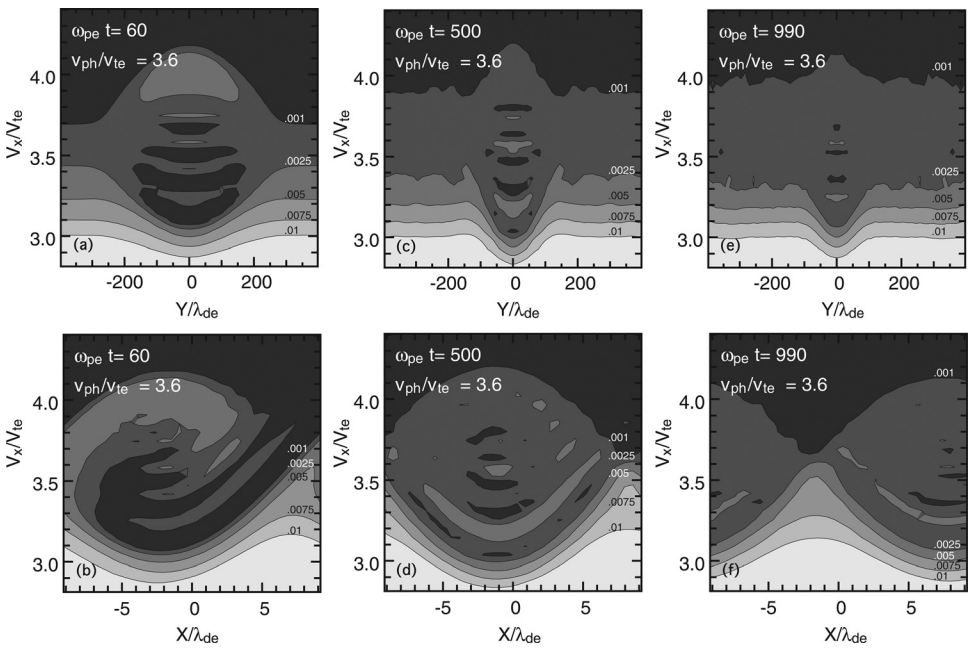

FIG. 10. The distribution of electrons shown in Fig 9. $F(V_x, Y)$ at the position of maximum potential for the EPW field and $F(V_x, X)$ at $y = 0$: (a) and (b) $\omega_{pe}t = 60$, (c) and (d) $\omega_{pe}t = 500$, (e) and (f) $\omega_{pe}t = 990$. The distribution is integrated over the transverse velocity. The phase velocity is $3.6\ V_{te}$.

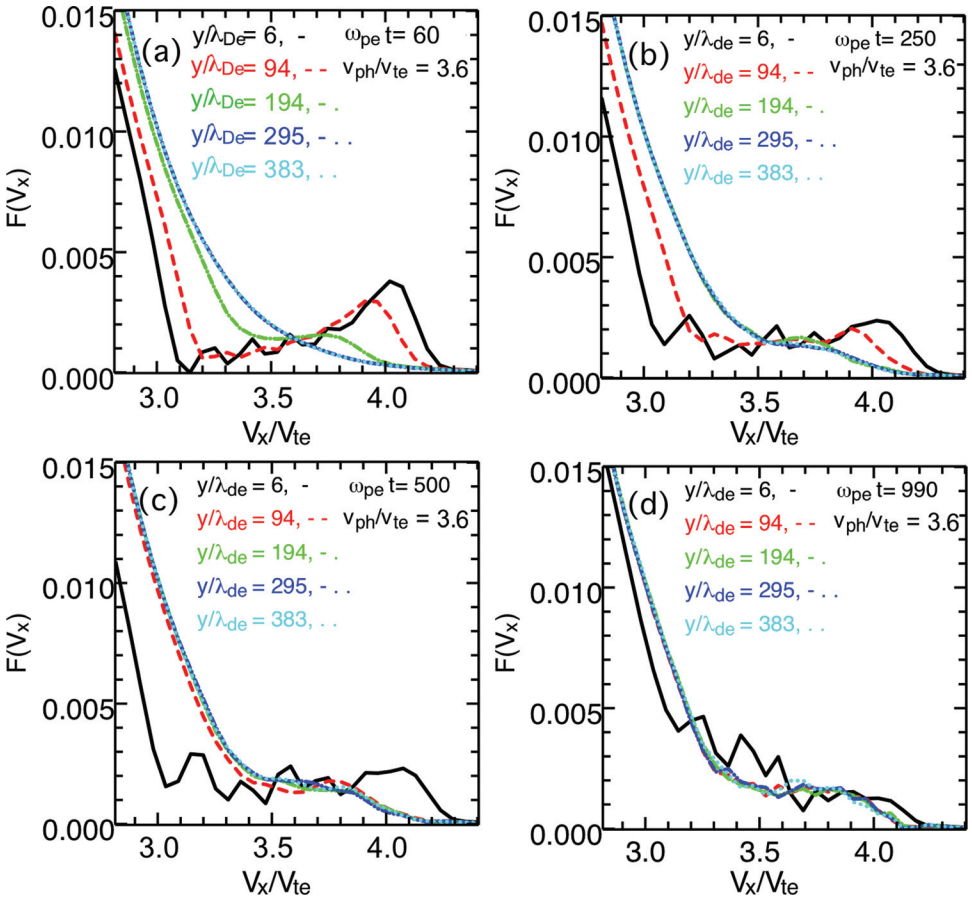

FIG. 11. (Color online) Lineouts of the distribution of electrons at the position of maximum potential for the EPW field shown in Fig. 9. and various y positions, $F(V_x)$ vs V_x at (a) $\omega_{pe}t = 60$, (b) $\omega_{pe}t = 250$, (c) $\omega_{pe}t = 500$, and (d) $\omega_{pe}t = 990$. The distribution is integrated over the transverse velocity. The phase velocity is 3.6 V_{te}. Note, the distributions for $y/\lambda_{De} = 295$ and $y/\lambda_{De} = 383$ are nearly the same.

region in physical space. At the final time shown, the distribution is becoming uniform transversely. The results with outflowing electron boundary conditions are the same until $\omega_{pe}t = 500$, after which the field amplitude continues to drop in time whereas, in the periodic case, the boundary condition stops the loss. The distribution at late times shows a reduced tail of trapped electrons but still a nearly uniform distribution as a function of the transverse spatial variable.

From the rate of decrease of the field energy with time for the simulations with outflowing electron boundary conditions, we can extract a field energy damping rate. The time-dependence of the field energy, $W_E = \int_{x,y} |E^2(x,y)| dxdy$, is fit to an exponential after the driver is off with the result, ν_t/ω_{pe}, given in the second column of Table I. The value does depend slightly on the time interval chosen. For the widest case that exhibited self-focusing, $\nu_t/\omega_{pe} = 0.0017$ if the fit extends to $1000\omega_{pe}^{-1}$ rather than to $800\omega_{pe}^{-1}$. The value of ν_t is even less sensitive to the time interval chosen for the other entries in Table I. This damping rate for the field energy is approximately $v_{te}/(4w_{fw})/\omega_{pe} = \lambda_{De}/(4w_{fw})$, the third column in Table I. In terms of the sideloss loss rate, $\nu_t \simeq \nu_{sl}/(8\sqrt{\ln 2})$, a remarkably good scaling especially given the facts that the sideloss rate is calculated from the driver transverse size and that the transverse size of the field is significantly different from the shape of the driving field. We also note that other factors, such as the phase velocity of the external field, have not been varied. Thus the field energy damping rate might well have other dependencies.

TABLE I. Transit damping rates.

w_{fw}/λ_{De}	ν_t/ω_{pe}	$\lambda_{De}/(4w_{fw})$
201	0.0013	0.0012
151	0.002	0.0017
94	0.0031	0.0027
52	0.0049	0.0048

V. CONCLUSIONS AND DISCUSSION

We have presented the results of 2D Vlasov electrostatic simulations of Langmuir waves driven to large amplitude by a traveling wave potential with a phase velocity several times the thermal velocity, $v_{ph}/v_{te} = 3.6$. The driving potential is given a spatial envelope transverse to the propagation direction to mimic the localization of the EPW in a laser speckle driven by stimulated Raman scattering. Our particular aims were to establish the conditions for which the phase fronts are curved in a focusing or defocusing manner and the effect of transverse convective loss of resonant, trapped electrons from the wave. These questions can be addressed with the modest-sized simulations that are one EPW wavelength long in propagation direction but up to 40 wavelengths in the transverse direction. The EPWs were driven at the linear Landau resonance of $\omega = 1.2\omega_{pe}$ for $k\lambda_{De} = 1/3$ over a relatively short time of about ten cycles.

In Sec. III, we established that a large-amplitude traveling EPW is produced in a BGK-like state for which the wave is weakly damped and resonant electrons cause a nonlinear frequency shift proportional to $\sqrt{e\phi/T_e}$. The frequency shift

magnitude and sign (negative) were shown to be in good agreement with the predictions of the theories of Dewar[4] and Morales and O'Neil.[5] For a slowly varying transverse profile of the EPW, the frequency shift is a function of the local value of the EPW amplitude. Thus the phase velocity of the wave is larger where the wave amplitude is smaller and, with time, the contours of constant phase curve more and more in a focusing sense in direction of the wave propagation. This is termed nonlinear wave bowing. For very small-amplitude waves, the frequency shift is insignificant, and the phase fronts curve backward (defocusing) with time because of the diffractive effects of EPW propagation in a finite temperature plasma. This is termed linear wave bowing. Nonlinear Langmuir wave bowing was previously shown by Rose and Yin[32] in PIC simulations to be a feature of SRS in speckled laser beams.

The diffractive effects are strong if the transverse size of the laser beam is small, whereas the frequency shifts are large when the wave amplitude is large. We have developed a quantitative measure (see Appendix A) that predicts which effect is dominant and have shown its validity by comparison with simulations. However, the resonant electrons that leave the wave by convecting laterally take energy from the wave. Other electrons that enter the wave laterally are, on average, accelerated and take energy from the wave but give part of it back as they leave. In Sec. IV, we showed by fitting the results of the simulations that the wave field energy effectively damps at about the sideloss rate, $v_{te}/(4\,w_{fw})$, where w_{fw} is the FWHM of the driving wave field lateral spatial profile. Another effect of the lateral motion of the resonant electrons is that the distribution of trapped electrons eventually becomes more uniform as a function of lateral distance from the peak wave amplitude. Thus, the number of trapped electrons is no longer a local function of the wave amplitude, and the nonlinear wave front bowing ceases to develop.

Because of nonlinear curvature of the phase fronts, trapped electron self-focusing is predicted to occur with a growth time of hundreds of $1/\omega_{pe}$.[31,32] In addition, the loss of field energy with time and the nonlocal relation of the frequency shift to the wave amplitude establish thresholds for Langmuir wave self-focusing. Most of our simulations shown in Sec. III were done for too short a time, too narrow an EPW, or too small an amplitude to show an increase in the wave amplitude on axis due to focusing. However, when the wave satisfies the conditions for "nonlinear bowing," the wave amplitude on axis drops much slower than the total field energy while the wave amplitude off axis drops faster than the total field energy. In Sec. IV, we show that a field with a wide enough initial spatial profile (thus weak transit damping losses) does increase its on-axis amplitude with a concomitant narrowing spatial profile if the conditions for nonlinear bowing are met. That is, trapped electron-induced self-focusing occurs.

As mentioned in the introduction, finite-amplitude EPWs may also be subject to various types of instabilities, such as the trapped particle instability (TPI; Ref. 66) or other modulational instabilities.[67] Our purely electrostatic simulations also preclude the possibility of electromagnetic instabilities, such as the Weibel instability, from which magnetic fields can grow.[68] The longitudinal electrostatic instabilities, involving sidebands, were unable to develop in the simulations presented in this paper as only single wavelength long systems in the longitudinal direction were considered. An obvious question is how the time scales over which these longitudinal instabilities may develop and break-up the original wave compared with the characteristic times of linear and nonlinear bowing studied in this paper. To systematically address this issue, multiple wavelength long simulations shall be carried out in the future. One may nonetheless attempt to estimate under what conditions the instability time scales might become comparable to bowing times. To this end, the reduced model for the TPI by Kruer, Dawson, and Sudan[66] was solved which has shown good semiquantitative agreement with fully kinetic simulations.[29,69] Their simple dispersion relation has three independent parameters: the wave number $k\lambda_{De}$ of the large amplitude EPW, the bounce-frequency ω_b, and the fraction f_t of trapped electrons. Consistent with the physical conditions for the simulations in this paper, one sets $k\lambda_{De}=1/3$ and $\omega_b/\omega_{pe}=k\lambda_{De}(e\phi/T_e)^{1/2}$ as is appropriate for the bounce frequency of deeply trapped electrons. Finally, the fraction of trapped electrons f_t is estimated by assuming a finite-amplitude, purely sinusoidal EPW and numerically integrating the electron distribution predicted by theory for sudden or adiabatic generation of the wave (as given by Eq. (1) or (4), respectively in Dewar's paper[4]). For $e\phi/T_e<1/8$, the number of trapped electrons for both distributions are approximately equal. The numerically computed TPI growth rate γ_{TPI} is well approximated by $\gamma_{TPI}\simeq\omega_b/8$ at least for our plasma parameters and the field amplitudes for which wave bowing and self-focusing were simulated. Assuming that the sidebands involved in the TPI must grow from thermal noise levels with an energy ratio of the finite EPW to noise of $\simeq n_e\lambda_{De}^3\sim 10^4$, one finds that approximately 4 e-folding times of the TPI are required for the sidebands to reach amplitudes that are comparable to the initial wave and break it up. One thus concludes that the characteristic time for sideband growth is of order, $t_{TPI}\simeq 32\omega_b^{-1}\simeq 100(e\phi/T_e)^{-1/2}\omega_{pe}^{-1}$.

For characteristic bowing times, let us consider the time $t_{1/4}$ at which the (absolute values) of linear (l) and nonlinear (nl) curvatures, given by Eqs. (16) and (17), respectively, reach the value $\frac{1}{4}$. This definition is based on the fact that, for the linear bowing case, this is the situation of maximum curvature. One thus has $t_{1/4}^{l}=t_{max}$ with t_{max} given by Eq. (18). For the nonlinear case, one obtains from (17),

$$\omega_{pe}\,t_{1/4}^{nl}=\frac{\omega_{pe}}{|\Delta\omega_{nl}|}=\frac{\sqrt{2\pi}}{\alpha}(k\lambda_{De})^2\frac{\exp(\frac{v^2}{2})}{v^2-1}\bigg|_{v=v_\phi/v_{th,e}}\left(\frac{e\phi_0}{T_e}\right)^{-1/2}.$$

Thus, the characteristic nonlinear bowing time $t_{1/4}^{nl}$ in fact presents the same scaling, $t_{1/4}^{nl}\sim\phi_0^{-1/2}$, in terms of the wave amplitude ϕ_0 as the growth time t_{TPI} of the TPI. Setting $k\lambda_{De}=1/3$, as considered for the simulations presented in this paper, one obtains $\omega_{pe}\,t_{1/4}^{nl}\simeq 13(e\phi_0/T_e)^{-1/2}$ (having used the Bohm–Grosss dispersion and assumed sudden wave generation, i.e., $\alpha=0.823$). From the above estimates, nonlinear bowing thus appears to develop before the TPI breaks up the wave, independent of wave amplitude. As demonstrated

in the simulations, and according to Eq. (19), for sufficiently low amplitudes ϕ_0 and narrow transverse widths Δy, the linear bowing time $t_{1/4}^{\mathrm{nl}}$ may be even shorter than the nonlinear bowing time, $t_{1/4}^{\mathrm{l}} < t_{1/4}^{\mathrm{nl}}$, but from these simple estimates, t_{TPI} is never the shortest time scale. One may thus conclude that both linear and nonlinear bowing of EPWs may be expected to be important features appearing in multidimensional and multiwavelength systems, such as relevant to SRS studies under laser-fusion conditions.

ACKNOWLEDGMENTS

This work was performed under the auspices of the U.S. Department of Energy by Lawrence Livermore National Laboratory under contract number DE-AC52-07NA27344. This work was funded by the Laboratory Directed Research and Development Program at LLNL under project tracking code 08-ERD-031. We acknowledge informative discussions with A. B. Langdon, W. B. Mori, D. Pesme, H. A. Rose, W. Rozmus, D. J. Strozzi, L. Yin, and B. Winjum.

APPENDIX A: WAVE FRONT BOWING IN THE LINEAR AND NONLINEAR LIMITS

In this appendix, we present calculations for the two-dimensional phase fronts expected for an undriven electron plasma wave in an infinite homogeneous plasma in the limits of (i) an arbitrarily small-amplitude wave and (ii) a large-amplitude wave in which a nonlinear frequency shift is assumed to dominate linear diffraction. These two limits are referred to as the linear and nonlinear regimes.

1. Wave evolution and bowing in the linear limit

One considers the evolution of a two-dimensional forward propagating EPW along the direction x, with a Gaussian transverse envelope. One thus assumes that at time $t=0$ the corresponding electrostatic potential $\phi(x,y,t=0)$ is given by

$$\phi(x,y,t=0) = A_0(y)\cos(kx), \tag{A1}$$

with $A_0(y)$ the Gaussian envelope,

$$A_0(y) = \phi_0 \exp\left[-\frac{1}{2}\left(\frac{y}{\Delta y}\right)^2\right],$$

with root mean square (rms) width Δy. To derive the subsequent time evolution of the wave field (A1), it is convenient to consider the corresponding plane wave, i.e., Fourier mode, decomposition,

$$\phi(x,y,t=0) = \int_{-\infty}^{+\infty} \hat{A}_0(k_y)\, e^{ik_y y}\, dk_y\ \frac{1}{2}\left(e^{ikx} + \mathrm{c.c.}\right)$$

where c.c. stands for the complex conjugate and $\hat{A}_0(k_y)$ is given by the Fourier transform of $A_0(y)$,

$$\hat{A}_0(k_y) = \frac{1}{2\pi}\int_{-\infty}^{+\infty} A_0(y) e^{-ik_y y}\, dy\ = \frac{\phi_0 \Delta y}{\sqrt{2\pi}} \exp\left[-\frac{1}{2}(k_y \Delta y)^2\right].$$

Then, making use of the linear dispersion relation for EPWs given by the Bohm–Gross relation, providing the wave frequency ω_K for a plane wave with wave vector $\vec{K}$,

$$\omega_K = \omega_{\mathrm{pe}}\left(1 + 3K^2\lambda_{\mathrm{De}}^2\right)^{1/2},$$

where ω_{pe} and λ_{De} stand, respectively, for the electron plasma frequency and Debye length, the electrostatic field at time t for the forward propagating wave can be written as

$$\phi(x,y,t) = \int_{-\infty}^{+\infty} dk_y \hat{A}_0(k_y)\frac{1}{2}\left[e^{i(kx+k_y y-\omega_K t)} + \mathrm{c.c.}\right], \tag{A2}$$

where for this last relation $K = (k^2 + k_y)^{1/2}$. Note that damping, in particular Landau damping, has been neglected. To obtain an explicit relation (A2), one Taylor expands the dispersion relation around k to second order in $k_y\lambda_{\mathrm{De}}$,

$$\omega_K \simeq \omega_k + \frac{3}{2}\frac{\omega_{\mathrm{pe}}^2}{\omega_k}(k_y\lambda_{\mathrm{De}})^2,$$

with $\omega_k = \omega_{\mathrm{pe}}(1 + 3k^2\lambda_{\mathrm{De}}^2)^{1/2}$. This should be a very good approximation, as the transverse envelope is typically many Debye lengths long, so that $k_y\lambda_{\mathrm{De}} \sim (\Delta y/\lambda_{\mathrm{De}})^{-1} \ll 1$. Making use of the relation

$$\int_{-\infty}^{+\infty} dk\, \exp(-\alpha k)^2\ =\ \frac{\sqrt{\pi}}{\alpha},$$

valid for any complex constant α such that $\mathrm{Re}(\alpha) > 0$, the integral over k_y in (A2) can be carried out analytically, leading to

$$\phi(x,y,t) = A(y,t)\cos\left[kx - \omega_k t + \frac{3}{2}\left(\frac{\lambda_{\mathrm{De}}}{\sigma(t)\Delta y}\right)^2\frac{\omega_{\mathrm{pe}}^2}{\omega_k}t\left(\frac{y}{\Delta y}\right)^2 - \theta\right], \tag{A3}$$

with the time evolving envelope $A(y,t)$ given by

$$A(y,t) = \frac{\phi_0}{\sqrt{\sigma(t)}}\exp\left[-\frac{1}{2}\left(\frac{y}{\sigma(t)\Delta y}\right)^2\right], \tag{A4}$$

and the phase factor θ such that

$$\tan(2\theta) = 3\left(\frac{\lambda_{\mathrm{De}}}{\Delta y}\right)^2\frac{\omega_{\mathrm{pe}}^2}{\omega_k}t.$$

According to (A4), the envelope remains Gaussian over time. The corresponding rms width is given by $\Delta y(t) = \sigma(t)\Delta y$, with

$$\sigma(t) = \left[1 + 9\left(\frac{\lambda_{\mathrm{De}}}{\Delta y}\right)^4\left(\frac{\omega_{\mathrm{pe}}}{\omega_k}\right)^2(\omega_{\mathrm{pe}}t)^2\right]^{1/2},$$

which thus asymptotically increases linearly in time. The time t_2 at which the rms width of the envelope has doubled is such that $\sigma(t_2) = 2$ and leads to

$$\omega_{\mathrm{pe}}t_2 = \frac{1}{\sqrt{3}}\left(\frac{\Delta y}{\lambda_{\mathrm{De}}}\right)^2\frac{\omega_k}{\omega_{\mathrm{pe}}}.$$

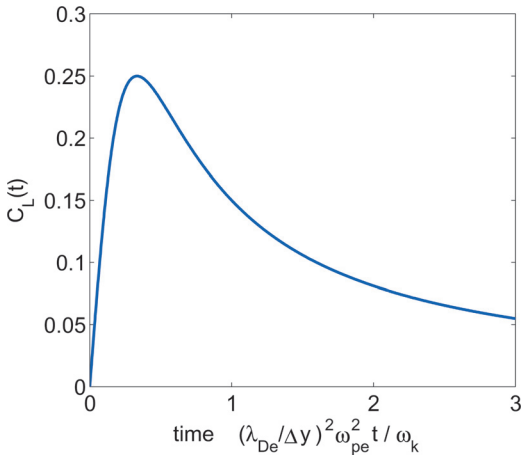

FIG. 12. (Color online) Time evolution of wave front curvature $|C_1(t)|$ resulting from linear dispersion of EPWs.

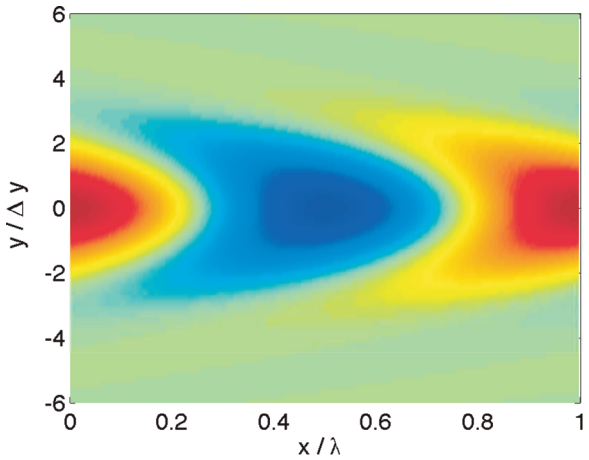

FIG. 13. (Color online) Electrostatic field $\phi(x,y)$ at time $t_{\max}$ where the negative curvature bowing resulting from the linear evolution is maximum.

According to Eq. (A3), all wavefronts (constant phase curves) are parallel to the parabolic curve $x=x(y)$ defined by

$$kx = -\frac{3}{2}\left(\frac{\lambda_{\mathrm{De}}}{\sigma(t)\Delta y}\right)^2 \frac{\omega_{\mathrm{pe}}^2}{\omega_k} t \left(\frac{y}{\Delta y}\right)^2 = C_1(t)\left(\frac{y}{\Delta y}\right)^2,$$

with the normalized curvature coefficient C_1 given by

$$C_1(t) = -\frac{3}{2}\left(\frac{\lambda_{\mathrm{De}}}{\sigma(t)\Delta y}\right)^2 \frac{\omega_{\mathrm{pe}}^2}{\omega_k} t. \tag{A5}$$

The subscript "l" stands for "linear" as the derived wavefront bowing results from the linear diffraction properties of the EPWs. Note that this linear curvature is negative. Its absolute value $|C_1(t)|$ increases, at first linearly, in time up to its maximum of 1/4 which is reached at time $t_{\max}$ given by

$$\omega_{\mathrm{pe}} t_{\max} = \omega_{\mathrm{pe}} t_2/\sqrt{3} = \frac{1}{3}\left(\frac{\Delta y}{\lambda_{\mathrm{De}}}\right)^2 \frac{\omega_k}{\omega_{\mathrm{pe}}}.$$

For times $t > t_{\max}$, the curvature $C_1(t)$ decreases and asymptotically in time vanishes. The time evolution of $|C_1(t)|$ is shown in Fig. 12. The electrostatic field $\phi(x,y)$ at time $t_{\max}$ where the negative curvature bowing resulting from the linear evolution is maximum is shown in Fig. 13.

2. Wave evolution and bowing in the nonlinear limit

According to Morales and O'Neil[5] and Dewar,[4] the nonlinear frequency shift $\Delta\omega_{\mathrm{nl}}$ for an EPW-type plane wave with finite relative density amplitude $\delta N/N$, N being the background electron density, is given by

$$\frac{\Delta\omega_{\mathrm{nl}}}{\omega_{\mathrm{pe}}} = -\frac{\alpha}{(k\lambda_{\mathrm{De}})^3}\left(\frac{\delta N}{N}\right)^{1/2} \frac{1}{\sqrt{2\pi}}(v^2-1)\exp\left(-\frac{v^2}{2}\right)\Big|_{v=v_\phi/v_{\mathrm{th,e}}}, \tag{A6}$$

having assumed a Maxwellian background, $v_\phi = \omega_k/k$ being the phase velocity relative to the wave number k, and $v_{\mathrm{th,e}} = (T_e/m_e)^{1/2}$ the thermal electron velocity. The frequency shift $\Delta\omega_{\mathrm{nl}}$ depends on how the finite-amplitude wave has been generated. This is reflected by the factor α, which takes on the two limiting values $\alpha^{\mathrm{adiab}} = 0.544$ and $\alpha^{\mathrm{sudden}} = 0.823$ depending on whether the wave has been turned on adiabatically or suddenly, respectively. The reference time scale for differentiating between these two limiting cases is the bounce frequency of (deeply) trapped electrons, given in the case of EPWs by $\omega_b/\omega_{\mathrm{pe}} = k\lambda_{\mathrm{De}}(e\phi_0/T_e)^{1/2} = (\delta N/N)^{1/2}$. A "sudden" wave is typically generated considering an initial value problem, while an "adiabatic" wave may be generated through an external drive which is sufficiently weak such that the characteristic growth time of the EPW remains small compared to ω_b^{-1}.

In the case of a two-dimensional finite-amplitude EPW of the form (A1), i.e., with transverse Gaussian envelope, the nonlinear frequency shift will vary together with the wave amplitude for different transverse positions y. Neglecting the linear diffraction effects discussed in Sec. A.1, in particular the spreading over time of the envelope, as well as damping effects, the evolution of the forward propagating wave including nonlinear frequency shift effects is given by

$$\phi(x,y,t) = A_0(y)\cos\{kx - [\omega_k + \Delta\omega_{\mathrm{nl}}(y)]t\}.$$

The corresponding wave fronts are thus all parallel to the curve $x=x(y)$ defined by

$$kx = \Delta\omega_{\mathrm{nl}}(y)t.$$

The transverse varying frequency shift $\Delta\omega_{\mathrm{nl}}(y)$ is given by Eq. (A6) with the factor $(\delta N/N)^{1/2}$ now being a function of y which is also essentially Gaussian [according to Poisson's equation $(\partial^2/\partial x^2 + \partial^2/\partial y^2)\,\phi = e\,\delta N/\epsilon_0$ and assuming $k\Delta y \ll 1$],

$$\left(\frac{\delta N(y)}{N}\right)^{1/2} \simeq \left(\frac{\delta N_0}{N}\right)^{1/2}\exp\left[-\frac{1}{4}\left(\frac{y}{\Delta y}\right)^2\right] \simeq \left(\frac{\delta N_0}{N}\right)^{1/2}\left[1-\frac{1}{4}\left(\frac{y}{\Delta y}\right)^2\right],$$

where $\delta N_0 = \delta N(y=0)$ and the last approximate equality is obtained as a result of a second-order Taylor expansion in $y/\Delta y$. The bowing of the wavefront resulting from the nonlinear frequency shift thus becomes

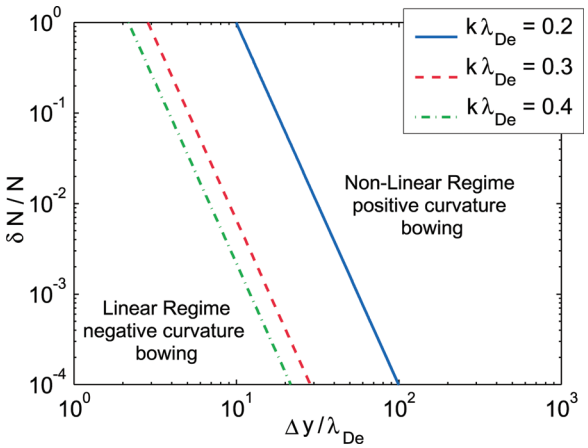

FIG. 14. (Color online) Critical curve in the $(\Delta y/\lambda_{De}, \delta N_0/N)$ plane delimiting the region corresponding to the linear regime with negative curvature of the wavefront for times $t \ll t_{max}$ from the nonlinear regime with positive curvature. Critical curves corresponding to the wavenumbers $k\lambda_{De} = 0.2$, 0.3, and 0.4 are shown, having used the Bohm–Gross dispersion and assumed an adiabatic generation of the EPWs.

$$kx = -\frac{1}{4}\frac{\Delta\omega_{nl,0}}{\omega_{pe}}\omega_{pe}t\left(\frac{y}{\Delta y}\right)^2 = C_{nl}(t)\left(\frac{y}{\Delta y}\right)^2,$$

with the normalized curvature coefficient C_{nl} defined by

$$C_{nl}(t) = -\frac{1}{4}\frac{\Delta\omega_{nl,0}}{\omega_{pe}}\omega_{pe}t, \tag{A7}$$

where $\Delta\omega_{nl,0}$ is given by Eq. (A6) evaluated for $(\delta N_0/N)^{1/2}$. Note that, as the nonlinear frequency shift is negative, the curvature C_{nl} is positive, i.e., of opposite sign to the curvature C_l resulting from the linear diffraction effects. Furthermore, contrary to $C_l(t)$, which vanished asymptotically in time, $C_{nl}(t)$ keeps on increasing linearly in time.

From relations (A5) and (A7), one may estimate for which conditions the negative curvature $C_l(t)$ of the wavefronts resulting from linear diffraction effects may be dominant over the positive curvature $C_{nl}(t)$ resulting from the nonlinear frequency shift, at least for times $t \ll t_{max}$ during which $C_l(t)$ evolves linearly in time. The condition $|C_l(t)| > C_{nl}(t)$ for $\omega_{pe}t \ll (\Delta y/\lambda_{De})^2$ leads to

$$\left(\frac{\delta N_0}{N}\right)^{1/2}\left(\frac{\Delta y}{\lambda_{De}}\right)^2 < \frac{6\sqrt{2\pi}}{\alpha}(k\lambda_{De})^3\frac{\exp(\frac{v^2}{2})}{(v^2-1)}\bigg|_{v=v_\phi/v_{th,e}},$$

which separates the $(\Delta y/\lambda_{De}, \delta N_0/N)$ plane into two domains, as shown in Fig. 14: (1) A small-amplitude, narrow-transverse-width domain where the linear diffraction effects dominate at early times and leading to negative curvature of the wave front. (2) A large-amplitude, wide-transverse-width domain where the nonlinear frequency shift effects dominate at all times, leading to positive curvature. Note that even in the linear regime region, the negative curvature ultimately vanishes after a sufficiently long time $t \gg t_{max}$, so that the positive curvature from the nonlinear effects can end up dominating asymptotically in time.

[1]J. H. Malmberg and C. B. Wharton, Phys. Rev. Lett. **19**, 775 (1967).
[2]P. Vidmar, J. H. Malmberg, and T. P. Starke, Phys. Rev. Lett. **34**, 646 (1975).
[3]W. Manheimer and R. Flynn, Phys. Fluids **14**, 2393 (1971).
[4]R. L. Dewar, Phys. Fluids **15**, 712 (1972).
[5]G. J. Morales and T. M. O'Neil, Phys. Rev. Lett. **28**, 417 (1972).
[6]A. Lee and G. Pocobelli, Phys. Fluids **15**, 2351 (1972).
[7]V. L. Bailey and J. Denavit, Phys. Fluids **13**, 451 (1970).
[8]J. Canosa and J. Gazdag, Phys. Fluids **17**, 2030 (1974).
[9]B. I. Cohen and A. N. Kaufman, Phys. Fluids **20**, 1113 (1977).
[10]J. F. Drake, P. K. Kaw, Y. C. Lee, G. Schmidt, C. S. Liu, and M. N. Rosenbluth, Phys. Fluids **17**, 778 (1974).
[11]W. L. Kruer, *The Physics of Laser Plasma Interactions* (Addison-Wesley, Redwood City, CA, 1988).
[12]A. Simon, R. W. Short, E. A. Williams, and T. Dewandre, Phys. Fluids **26**, 3107 (1983).
[13]W. Seka, D. H. Edgell, J. F. Myatt, A. V. Maximov, R. W. Short, V. N. Goncharov, and H. A. Baldis, Phys. Plasmas **16**, 052701 (2009).
[14]S. P. Regan, N. B. Meezan, L. J. Suter, D. J. Strozzi, W. L. Kruer, D. Meeker, S. H. Glenzer, W. Seka, C. Stoeckl, V. Y. Glebov, T. C. Sangster, D. D. Meyerhofer, R. L. McCrory, E. A. Williams, O. S. Jones, D. A. Callahan, M. D. Rosen, O. L. Landen, C. Sorce, and B. J. MacGowan, Phys. Plasmas **17**, 020703 (2010).
[15]J. D. Lindl, *Inertial Confinement Fusion* (AIP Press, Springer, New York, 1998).
[16]J. Lindl, P. Amendt, R. L. Berger, S. G. Glendinning, S. H. Glenzer, S. Haan, R. L. Kauffman, O. Landen, and L. J. Suter, Phys. Plasmas **11**, 339 (2004).
[17]N. B. Meezan, L. J. Atherton, D. A. Callahan, E. L. Dewald, S. Dixit, E. G. Dzenitis, M. J. Edwards, C. A. Haynam, D. E. Hinkel, O. S. Jones, O. L. Landan, R. A. London, P. Michel, J. D. Moody, J. Milovich, M. B. Schneider, C. A. Thomas, R. P. J. Town, A. L. Warrick, S. Weber, K. Widmann, S. H. Glenzer, L. J. Suter, B. J. MacGowan, J. L. Kline, G. A. Kyrala, and A. Kikroo, Phys. Plasmas **17**, 056304 (2010).
[18]S. Glenzer, B. MacGowan, P. Michel, N. Meezan, L. Suter, S. Suter, S. Dixit, J. Kline, G. Kyrala, D. Bradley, D. A. Callahan, E. L. Dewald, L. Divol, E. Dzenitis, M. J. Edwards, A. V. Hamza, C. A. Haynam, D. E. Hinkel, D. H. Kalantar, J. D. Kilkenny, O. L. Landen, J. D. Lindl, S. LePape, J. D. Moody, A. Nikroo, T. Parham, M. B. Schneider, R. P. J. Town, P. Wegner, K. Widmann, P. Whitman, B. K. F. Young, B. V. Wonterghem, L. J. Atherton, and E. I. Moses, Science **327**, 1228 (2010).
[19]D. Froula, L. Divol, R. London, R. Berger, T. Doppner, N. Meezan, J. Ross, L. Suter, C. Sorce, and S. Glenzer, Phys. Rev. Lett. **103**, 045006 (2009).
[20]D. H. Froula, L. Divol, R. A. London, R. L. Berger, T. Doppner, N. B. Meezan, J. Ralph, J. S. Ross, L. J. Suter, and S. H. Glenzer, Phys. Plasmas **17**, 056302 (2010).
[21]D. E. Hinkel, D. A. Callahan, A. B. Langdon, S. H. Langer, C. H. Still, and E. A. Williams, Phys. Plasmas **15**, 012702 (2008).
[22]S. Laffite and P. Loiseau, Phys. Plasmas **17**, 102704 (2010).
[23]D. S. Clark and N. J. Fisch, Phys. Plasmas **10**, 3363 (2003).
[24]R. L. Berger, C. H. Still, E. A. Williams, and A. B. Langdon, Phys. Plasmas **5**, 4337 (1998).
[25]D. J. Strozzi, private communication (2010).
[26]M. V. Goldman, Rev. Mod. Phys. **56**, 709 (1984).
[27]R. P. Drake and S. H. Batha, Phys. Fluids B **3**, 2936 (1991).
[28]J. P. Palastro, E. A. Williams, D. E. Hinkel, L. Divol, and D. J. Strozzi, Phys. Plasmas **16**, 092304 (2009).
[29]S. Brunner and E. J. Valeo, Phys. Rev. Lett. **93**, 145003 (2004).
[30]L. Yin, B. J. Albright, K. J. Bowers, W. Daughton, and H. A. Rose, Phys. Rev. Lett. **99**, 265004 (2007a).
[31]H. A. Rose, Phys. Plasmas **12**, 012318 (2005).
[32]H. A. Rose and L. Yin, Phys. Plasmas **15**, 042311 (2008).
[33]C. K. Birdsall and A. B. Langdon, *Plasma Physics via Computer Simulation*, 2nd ed., The Adam Hilger Series on Plasma Physics (Adam Hilger, New York, 1991).
[34]C. Z. Cheng and G. Knorr, J. Comput. Phys. **22**, 330 (1976).
[35]M. M. Shoucri and R. R. J. Gagné, J. Comput. Phys. **27**, 315 (1978).
[36]A. Ghizzo, B. Izrar, P. Bertrand, E. Fijalkow, M. R. Feix, and M. Shoucri, Phys. Fluids **31**, 72 (1988).
[37]P. Bertrand, A. Ghizzo, T. W. Johnson, M. Shoucri, E. Fijalkow, and M. R. Feix, Phys. Fluids B **2**, 1028 (1990).
[38]The simulations used the approximation to the Gaussian given by $A(y) = cos^2(2\pi k_y y/F_y)$ with $F_y = 10\Delta y$. For $|y| > F_y/4, A(y) = 0$.
[39]H. A. Rose and D. A. Russell, Phys. Plasmas **8**, 4784 (2001).

[40]L. Yin, B. J. Albright, K. J. Bowers, W. Daughton, and H. A. Rose, Phys. Rev. Lett. **99**, 265004 (2007b).
[41]L. Yin, B. J. Albright, H. A. Rose, K. J. Bowers, B. Bergen, D. S. Montgomery, J. L. Kline, and J. C. Fernandez, Phys. Plasmas **16**, 113101 (2009).
[42]T. M. O'Neil, Phys. Fluids **8**, 2255 (1965).
[43]D. S. Montgomery, J. Cobble, J. C. Fernandez, R. Focia, R. Johnson,N. Renard-LeGalloudec, H. A. Rose, and D. Russell, Phys. Plasmas **9**, 2311 (2002).
[44]P. Colella, M. R. Dorr, J. A. F. Hittinger, P. McCorquodale, and D. F. Martin, in *Numerical Modeling of Space Plasma Flows: Astronum 2008*, Astronomical Society of the Pacific Conference Series, Vol. 406, edited by N. V. Pogorelov, E. Audit, P. Colella, and G. P. Zank (Astronomical Society of the Pacific, San Francisco, 2009), pp. 207–216.
[45]P. Colella, M. R. Dorr, J. A. F. Hittinger, and D. F. Martin, J. Comput. Phys. **230**, 2952 (2011).
[46]J. W. Banks and J. A. F. Hittinger, IEEE Trans. Plasma Sci. **38**, 2198 (2010).
[47]C.-W. Shu, "Essentially non-oscillatory and weighted essentially non-oscillatory schemes for hyperbolic conservation laws," Tech. Rep. NASA-CR-97-206253 (NASA Langley Research Center, 1997).
[48]A. K. Henrick, T. D. Aslam, and J. M. Powers, J. Comput. Phys. **207**, 542 (2005).
[49]U. M. Ascher and L. R. Petzold, *Computer Methods for Ordinary Differential Equations and Differential-Algebraic Equations* (SIAM, Philadelphia, 1998).
[50]Overture and Team, "Overture home page," Tech. Rep. UCRL-MI-134872 http://www.llnl.gov/CASC/Overture (Lawrence Livermore National Laboratory, 2006).
[51]W. D. Henshaw, "Ogen: An overlapping grid generator for Overture," Research Report UCRL-MA-132237 (Lawrence Livermore National Laboratory, 1998).
[52]Y. Saad and M. H. Schultz, SIAM J. Sci. Stat. Comput. **7**(4), 856 (1986).
[53]R. C. Davidson, *Methods in Nonlinear Plasma Theory* (Academic, New York, 1972).
[54]R. Dewar and J. Lindl, Phys. Fluids **15**, 820 (1972).
[55]T. Coffey, Phys. Fluids **14**, 1402 (1971).
[56]B. Winjum, J. Fahlen, and W. Mori, Phys. Plasmas **14**, 102104 (2007).
[57]R. L. Berger, S. Brunner, L. Divol, C. H. Still, and E. J. Valeo, Phys. Plasmas "Electron and Ion Kinetic Effects on Nonlinearly Driven Electron Plasma and Ion Acoustic Waves," Tech. Rep. LLNL-JRNL-480183 (Lawrence Livermore National Laboratory, 2011).
[58]D. Benisti and L. Gremillet, Phys. Plasmas **14**, 042304 (2007).
[59]D. Benisti, D. J. Strozzi, and L. Gremillet, Phys. Plasmas **15**, 030701 (2008).
[60]D. Benisti, O. Morice, L. Gremillet, E. Siminos, and D. J. Strozzi, Phys. Plasmas **17**, 102311 (2010).
[61]A detailed discussion of this technique is given in Berger, *et al*. (Ref. 57)
[62]D. J. Strozzi, E. A. Williams, H. A. Rose, D. E. Hinkel, and A. B. Langdon, private communication (2010).
[63]H. A. Rose, private communication (2010).
[64]J. Fahlen, B. Winjum, T. Grismayer, and W. Mori, Phys. Rev. E **83**, 045401(R) (2011).
[65]G. Manfredi, Phy. Rev. Lett. **79**, 2815 (1997).
[66]W. L. Kruer, J. M. Dawson, and R. N. Sudan, Phys. Rev. Lett. **23**, 838 (1969).
[67]R. L. Dewar, W. L. Kruer, and W. M. Manheimer, Phys. Rev. Lett. **28**, 215 (1972).
[68]P.-E. Masson-Laborde, W. Rozmus, Z. Peng, D. Pesme, S. Huller, M. Casanova, V. Y. Bychenkov, T. Chapman, and P. Loiseau, Phys. Plasmas **17**, 092704 (2010).
[69]In general, transverse modulations must also be considered in which case the growth rate could double but our conclusion that the bowing timescale is shorter than the modulation timescale remains valid.